



Supervised machine learning on Galactic filaments. Revealing the filamentary structure of the Galactic interstellar medium

A. Zavagno, F. -X. Dupé, S. Bensaid, E. Schisano, G. Li Causi, M. Gray, S.
Molinari, D. Elia, J. -C. Lambert, M. Brescia, et al.

► To cite this version:

A. Zavagno, F. -X. Dupé, S. Bensaid, E. Schisano, G. Li Causi, et al.. Supervised machine learning on Galactic filaments. Revealing the filamentary structure of the Galactic interstellar medium. Astronomy and Astrophysics - A&A, 2023, 669, 10.1051/0004-6361/202244103 . insu-03967851

HAL Id: insu-03967851

<https://insu.hal.science/insu-03967851>

Submitted on 2 Feb 2023

HAL is a multi-disciplinary open access archive for the deposit and dissemination of scientific research documents, whether they are published or not. The documents may come from teaching and research institutions in France or abroad, or from public or private research centers.

L'archive ouverte pluridisciplinaire **HAL**, est destinée au dépôt et à la diffusion de documents scientifiques de niveau recherche, publiés ou non, émanant des établissements d'enseignement et de recherche français ou étrangers, des laboratoires publics ou privés.



Distributed under a Creative Commons Attribution 4.0 International License

Supervised machine learning on Galactic filaments

Revealing the filamentary structure of the Galactic interstellar medium

A. Zavagno^{1,2}, F.-X. Dupé^{3,*}, S. Bensaid^{1,3,*}, E. Schisano⁴, G. Li Causi⁴, M. Gray¹, S. Molinari⁴, D. Elia⁴, J.-C. Lambert¹, M. Brescia⁵, D. Arzoumanian^{1,6}, D. Russeil¹, G. Riccio⁵, and S. Cuvuoti⁵

¹ Aix-Marseille Univ, CNRS, CNES, LAM, 38 rue F. Joliot-Curie, 13013 Marseille, France
e-mail: annie.zavagno@lam.fr

² Institut Universitaire de France, Paris, France

³ Aix-Marseille Univ, CNRS, LIS, Ecole Centrale Marseille, 38 rue F. Joliot-Curie, 13013 Marseille, France

⁴ INAF-IAPS, via del Fosso del Cavaliere 100, 00133 Roma, Italy

⁵ INAF – Astronomical Observatory of Capodimonte, via Moiariello 16, 80131, Napoli, Italy

⁶ Division of Science, National Astronomical Observatory of Japan, 2-21-1 Osawa, Mitaka, Tokyo 181-8588, Japan

Received 24 May 2022 / Accepted 20 November 2022

ABSTRACT

Context. Filaments are ubiquitous in the Galaxy, and they host star formation. Detecting them in a reliable way is therefore key towards our understanding of the star formation process.

Aims. We explore whether supervised machine learning can identify filamentary structures on the whole Galactic plane.

Methods. We used two versions of UNet-based networks for image segmentation. We used H₂ column density images of the Galactic plane obtained with *Herschel* Hi-GAL data as input data. We trained the UNet-based networks with skeletons (spine plus branches) of filaments that were extracted from these images, together with background and missing data masks that we produced. We tested eight training scenarios to determine the best scenario for our astrophysical purpose of classifying pixels as filaments.

Results. The training of the UNets allows us to create a new image of the Galactic plane by segmentation in which pixels belonging to filamentary structures are identified. With this new method, we classify more pixels (more by a factor of 2 to 7, depending on the classification threshold used) as belonging to filaments than the spine plus branches structures we used as input. New structures are revealed, which are mainly low-contrast filaments that were not detected before. We use standard metrics to evaluate the performances of the different training scenarios. This allows us to demonstrate the robustness of the method and to determine an optimal threshold value that maximizes the recovery of the input labelled pixel classification.

Conclusions. This proof-of-concept study shows that supervised machine learning can reveal filamentary structures that are present throughout the Galactic plane. The detection of these structures, including low-density and low-contrast structures that have never been seen before, offers important perspectives for the study of these filaments.

Key words. methods: statistical – stars: formation – ISM: general

1. Introduction

The *Herschel* infrared Galactic Plane Survey, Hi-GAL (Molinari et al. 2010), revealed that the cold and warm interstellar medium (ISM) is organized in a network of filaments in which star formation is generally observed above a density threshold corresponding to $A_V=7$ mag (André et al. 2014; Könyves et al. 2020). The most massive stars are formed at the junction of the densest filaments, called hubs (Kumar et al. 2020). Because filaments host star formation and link the organization of the interstellar matter to the future star formation, studying them is central to our understanding of all properties related to star formation, such as the initial mass function, the star formation rate, and the star formation efficiency. Filaments are therefore extensively studied with observations at all wavelengths and numerical simulations (André et al. 2010; Molinari et al. 2010; Arzoumanian et al. 2011, 2019; Hacar et al. 2018, 2022; Shimajiri et al. 2019; Clarke et al. 2020; Priestley & Whitworth 2022, and references therein). All these data

reveal the complex structure of filaments and show a changing morphology, depending on the way (resolution or tracers) in which they are observed (Leurini et al. 2019). For example, high-resolution molecular line observations of Galactic filaments with the Atacama Large Millimeter Array (ALMA) show that they are made of fibers on a spatial scale <0.1 pc (Shimajiri et al. 2019; Hacar et al. 2018). Their complex morphology and dynamics are also revealed with 3D spectroscopic information (Mattern et al. 2018; Hacar et al. 2020) and show their key role in the accretion process from large (>10 pc) to subparsec scales, funnelling material down to the star-forming cores. However, the way filaments form and evolve in the ISM is still debated (Hoemann et al. 2021; Hsieh et al. 2021). Recent results suggest that compression from neutral (H I) and ionized (H II) shells could play an important role in forming and impacting the evolution of Galactic filaments (Zavagno et al. 2020; Bracco et al. 2020). Their detection in nearby galaxies, where they are also clearly linked to the star formation process, makes studying filaments even more important and universal (Fukui et al. 2019).

Different algorithms are used to extract filaments from 2D images (Sousbie 2011; Schisano et al. 2014, 2020; Koch & Rosolowsky 2015; Zucker & Chen 2018; Men'shchikov 2021)

* F.-X. Dupé and S. Bensaid contributed equally to the work presented in this article.

and from 3D spectral data cubes (Sousbie 2011; Chen et al. 2020). These algorithms often rely on a threshold definition (for intensity or column density). Nonetheless, a close visual inspection of 2D images and 3D cubes show that some filaments are missed by all these detection algorithms, especially when the filaments have low column density contrasts. This means that even large surveys of the Galactic plane cannot deliver a complete (unbiased) view of the filaments present there. Another limitation of these algorithms comes from their computation time, which can make some of them too expensive to envision a complete run on large-scale surveys data for multiple defined threshold and extraction parameters. Because the multi-wavelength information available on our Galaxy on all spatial scales is so rich, proposing another way of extracting filaments might allow a leap forward for an unbiased census of these data. In this paper, we explore the potential of supervised machine learning as a new way to reveal filaments from 2D images. Using Hi-GAL data, Schisano et al. (2020) extracted filaments from column density (N_{H_2}) images of the Galactic plane. Based on these data, we study the possibility for convolutional UNet-based networks (Fu & Mui 1981) to identify pixels as belonging to the filament class, based on the input information given as previously identified filament masks from Schisano et al. (2020). Except for the catalog of filament candidates published in Schisano et al. (2020) where faint filaments present in the Galactic plane are known to be missed, no complete extraction of filamentary structures in the Galactic plane exists so far. This fact motivates our work, in which we propose an alternative method that could allow us to go beyond the current possibilities. However, this fact also indicates that we worked with an incomplete ground truth (see Sect. 2.2) that renders an absolute evaluation of the method performances proposed here impossible. Nonetheless, we show that new filaments revealed by the UNet-based algorithm and not detected before are confirmed through imaging at other wavelengths, which gives us confidence that this new method can progress toward an unbiased detection of filaments.

The paper is organized as follows: in Sect. 2 we describe the images and the information on the filament locations we used in the supervised learning. The supervised learning itself is described in Sect. 3. Results are presented in Sect. 4 and are discussed in Sect. 5. Conclusions are given in Sect. 6.

2. Data

2.1. Hi-GAL catalog

The *Herschel* infrared Galactic Plane Survey, Hi-GAL (Molinari et al. 2010), is a complete survey of the Galactic plane performed in five infrared photometric bands centered at 70, 160, 250, 350, and 500 μm . H_2 column density (N_{H_2}) images were created for the whole Galactic plane following the method described in Elia et al. (2013) and Schisano et al. (2020). N_{H_2} and dust temperature maps were computed from photometrically calibrated images. The *Herschel* data were convolved to the 500 μm resolution ($36''$), and a pixel-by-pixel fitting by a single-temperature graybody was performed. An example of the column density image covering the $l = 349\text{--}356^\circ$ region is presented in Fig. 1. This region contains the bright and well-studied Galactic star-forming regions NGC 6334 and NGC 6357.

Schisano et al. (2020) analyzed the whole Galactic plane by extracting filamentary structures from the H_2 column density (N_{H_2}) maps. In their work, a filament is defined as a two-dimensional, cylindric-like structure that is elongated and shows

a higher brightness contrast with respect to its surroundings. The extraction algorithm is based on the Hessian matrix $H(x, y)$ of the intensity map $N_{\text{H}_2}(x, y)$ to enhance elongated regions with respect to any other emission. The algorithm performs a spatial filtering and amplifies the contrast of small-scale structures in which the emission changes rapidly. Further filtering allows identifying the filamentary structures. Figure 2 shows an example of this filament extraction, reproducing the Fig. 3 of Schisano et al. (2020). We chose this figure because it shows the input we use in this work: the spine (blue line) and the branches (red lines, both shown in the bottom left panel) associated with a given filament. Schisano et al. (2020) defined a filament as traced by its associated region of interest (RoI; bottom right), which covers a larger area than the region that is defined with the spine plus branches. In this work we use this spine plus branches structure to define a filament because the early tests we made to train the networks with the input RoIs returned filamentary structures that were too large compared to the structure that is observed in the column density mosaics. This point is illustrated in Fig. 21 and is discussed in Sect. 4.3.

The analysis of the extracted structures from Schisano et al. (2020) resulted in the publication of a first catalog of 32 059 filaments that were identified over the entire Galactic plane. We used this published catalog of filaments and their associated spine plus branches as ground truth of the filament class for the training process (see Sect. 2.2). The method is described in Sect. 3.

2.2. Data preprocessing

As methods based on deep learning strongly depend on the nature and on the representativity of the input data, we took particular attention to the construction of the data set. We used four input maps (see Fig. 3): (1) the N_{H_2} mosaics obtained as part of the Hi-GAL survey products (Molinari et al. 2016; Schisano et al. 2020, e.g., Fig. 1), (2) the spines plus branches of the detected filaments from Schisano et al. (2020, e.g., Fig. 2 bottom left corner), (3) a background map (localization of nonfilament pixels), and (4) a missing-data map (see Appendix A). The origin and the ways in which these maps were obtained are presented in Appendix A. An example of these maps is given on Fig. 3, illustrated for the two portions of the Galactic plane that are located at $160\text{--}171^\circ$ and $349\text{--}356^\circ$. We obtained results for the whole Galactic plane, which we illustrate in two regions that we selected because they represent the diversity of column density and filaments content observed in the Galactic plane well. The $160\text{--}171^\circ$ region samples a low column density medium (up to $8 \times 10^{21} \text{ cm}^{-2}$) in which only a few filaments are detected, while the $349\text{--}356^\circ$ region shows a rich content in filaments that are detected in a high column density medium (up to $9 \times 10^{22} \text{ cm}^{-2}$, see Fig. 3). For the training step, we merged all the individual mosaics (10° -long in longitude direction) into one global map using the *reproject* module for *astropy* (Robitaille et al. 2020, and Appendix A).

As the four input maps are very large ($150\,000 \times 2000$ pixels), we split them into many patches that constitute the original data set. As shown in Fig. 4, we split the maps into $p \times p$ patches. The size of $p = 32$ pixels was chosen to preserve the information on the small filamentary structures. This size is also the minimum size accepted by the UNet architecture. The patches were generated by applying a sliding window of size p (the patch size) to the global mosaic of H_2 column density (N_{H_2}). To ensure the coherence between the four input maps, the four patches (N_{H_2} , spine+branches, background, and missing data) were taken using the same coordinates (see Fig. 5). In order to avoid any common

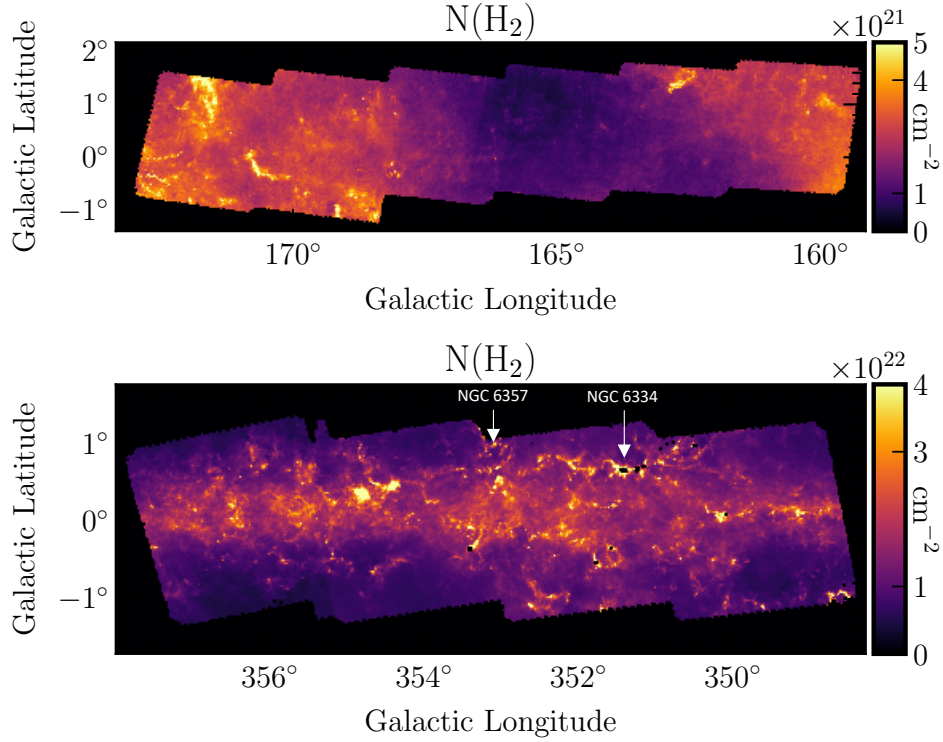


Fig. 1. Hi-GAL H_2 column density image of the $l = 160\text{--}171^\circ$ (top) and $l = 349\text{--}356^\circ$ (bottom) regions produced using Hi-GAL images as described in [Elia et al. \(2013\)](#). The $l = 349\text{--}356^\circ$ zone contains the bright star-forming regions NGC 6334 and NGC 6357. These two regions are used in this paper to illustrate the results. The dark pixels are saturated.

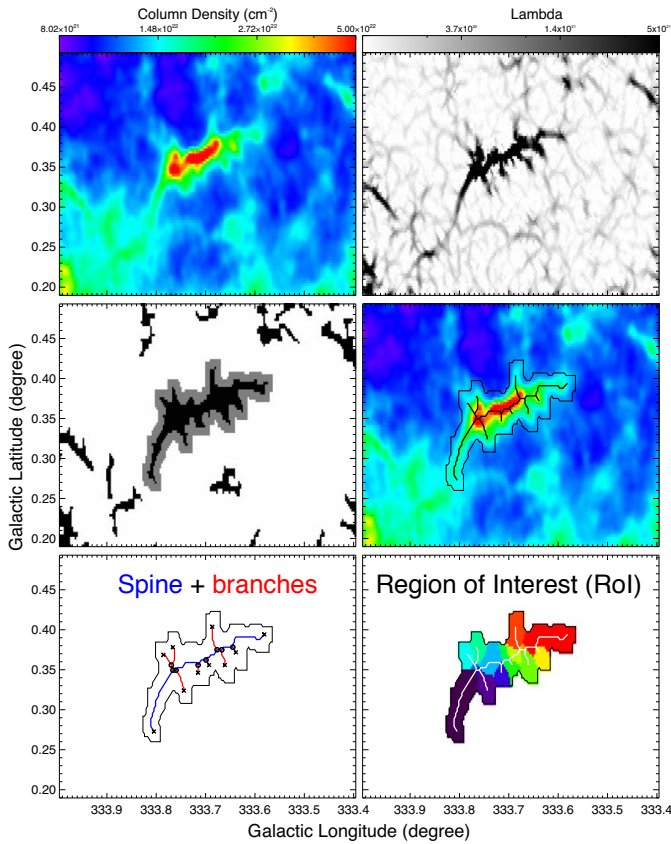


Fig. 2. Illustration of the filament extraction method from [Schisano et al. \(2020, their Fig. 3\)](#). The spine (blue line) and branches (red lines) associated with a filament used for the supervised training process are shown in the bottom left corner. The RoI (bottom right corner) is the zone used by [Schisano et al. \(2020\)](#) to define a filament.

information between patches, the construction was made without any overlap between the patches.

2.3. Data augmentation

Deep neural networks are greedy algorithms. In spite of the huge size of the Galactic map, the final data set had merely 52 000 patches after empty patches were removed. Here, we refer as “empty patches” to patches that only contain missed values (patches located on edges) or to patches that contain “0 pixels labeled data”. Fully unlabeled patches were removed from the patch data set. As unlabeled pixels represent more than 80% of the data set, this resulted in the loss of many patches. The data augmentation is thus necessary in order to increase the number of training and validation patches and to thereby enable a sufficient convergence of the neural network during the training step ([Goodfellow et al. 2016](#)). Two types of rotation were used: rotation around the central pixel of the squared patch (0° (original), 90° , 180° , and 270°), and flipping the patch with respect to the x - and y -axes. We also allowed a composition of both rotations. All possible transformations are equally probable, that is, we selected the applied transformation following a uniform distribution. To attenuate redundancy issues, the augmentation was done on the fly, meaning that at each batch, we produced a new set of patches using the augmentation process. With our setting, we virtually increased the number of patches by a factor equal to 64. Figure 6 shows some examples of the data augmentation process.

3. Method

3.1. Segmentation pipeline

Our segmentation method relies on three components: a data preparation procedure, a neural network with an architecture

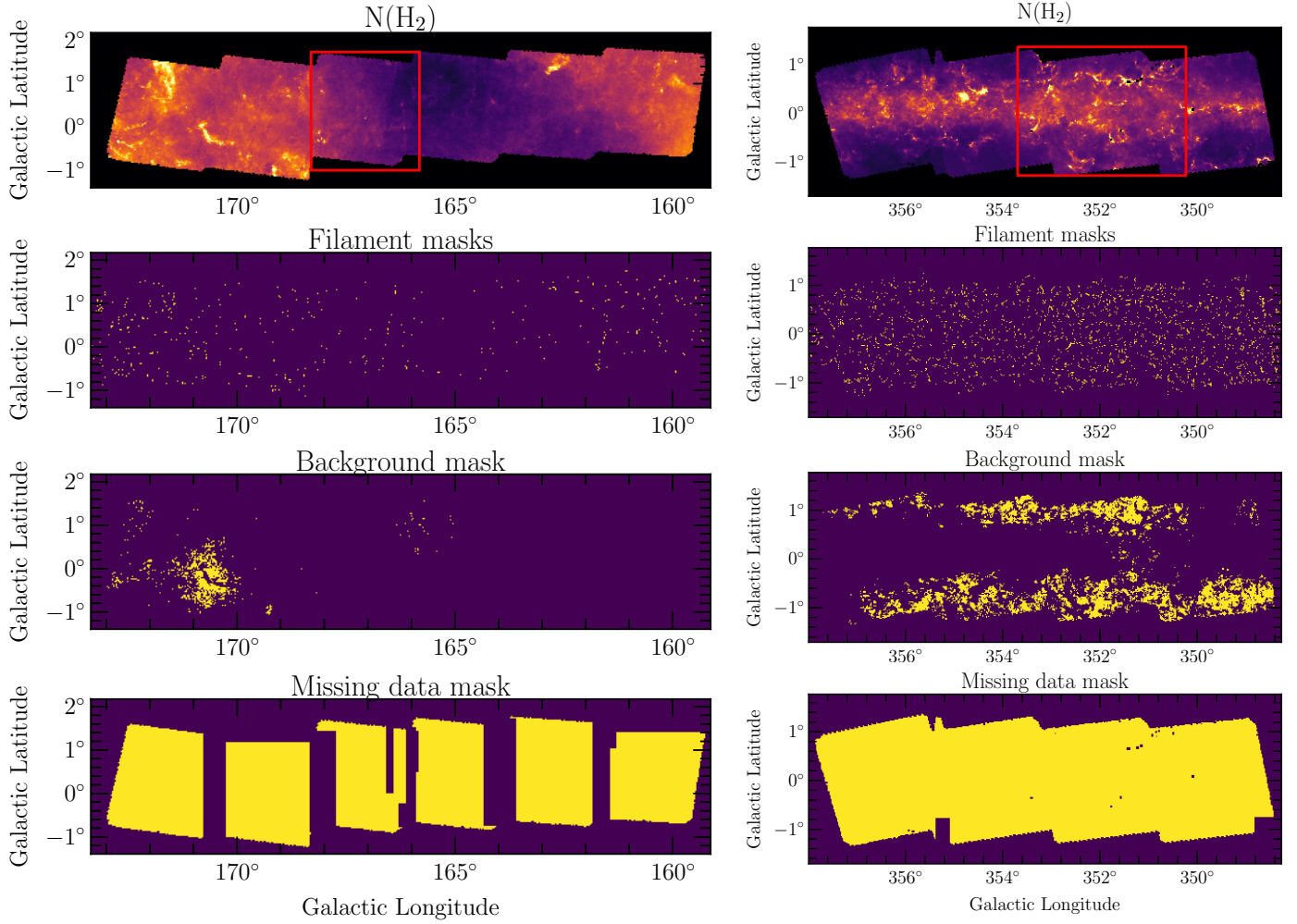


Fig. 3. Illustration of the Galactic regions located at 160–171° (left) and 349–356° (right) of the four input maps used for the supervised learning. From top to bottom, we show the N_{H_2} column density map, the input filament masks, a background localization map, and the missing-data map (0 in purple, 1 in yellow). All these maps were obtained as explained in Appendix A. The filament and background mask maps are multiplied by the missing-data map before they were used in the training process. The red rectangle shown in each column density map represents the region we extracted to compute the performance of the training (see Sect. 4.1).

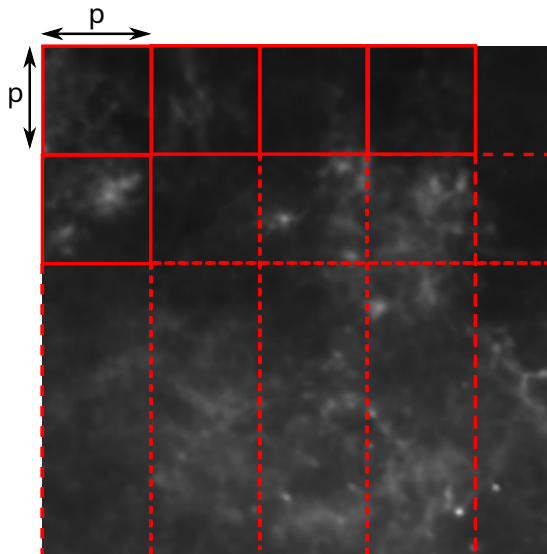


Fig. 4. Construction of patches of size $p \times p$ using a sliding window.

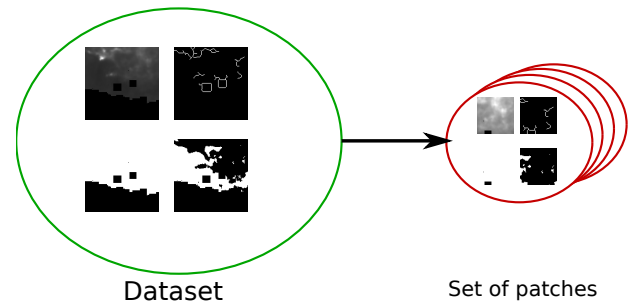


Fig. 5. Building the data set using the four input maps (on the left) into a set of patches (on the right). On the left, the maps are the column density (top left), filament spine+branches (top right), missing data (bottom left), and background pixels (bottom right).

dedicated to the recognition of filamentary structures, and a training procedure adapted to the N_{H_2} data. After the neural network was trained, we used it to segment the N_{H_2} map. The result of the segmentation process is a map in which the pixels are

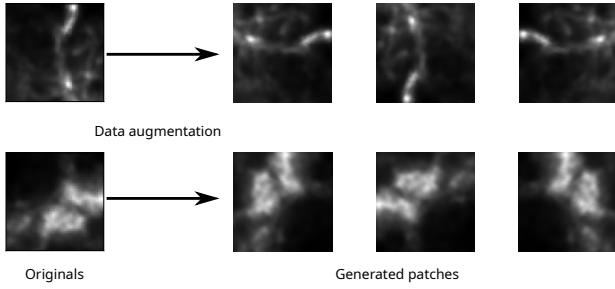


Fig. 6. Example of data augmentation results.

classified into two classes: either a filament pixel (identified as class 1), or a background pixel (identified as class 0). With these two classes, we produced an intensity map with values of 0 and 1. The values of the classification indicate whether a pixel belongs to the filament class (the reverse map shows the classification value according to which a pixel belongs to the background class).

3.1.1. Segmentation with UNets

Automatic segmentation is a well-known issue in the artificial intelligence community. Its origins lie in computer vision. It is a well-studied problem today, especially where segmentation is mandatory for decision or prediction, typically for medical or biology images (Fu & Mui 1981; Alzahrani & Boufama 2021). It has also been used for a long time in astrophysics, with recent applications on galaxies (Zhu et al. 2019; Hausen & Robertson 2020; Bianco et al. 2021; Bekki 2021). Most previous methods are based on classical machine-learning methods, such as Support-Vector Machine (SVM) or Random Forest (Hastie et al. 2001). These methods must extract an adapted set of features in order to be sufficiently efficient: we have to be sure that the extracted features represent the subject we wish to study well. These features are usually given by expert knowledge of the problem.

Most successful machine-learning methods for image processing tasks today are based on deep neural network methods (Goodfellow et al. 2016). These methods have the particularity of learning both the task and a representation of the data dedicated to the task itself. Thus, they are more powerful than methods based on hand-tuned features. While the first methods were dedicated to classification (e.g., AlexNet, Krizhevsky et al. 2012; LeNet, LeCun et al. 1989; or ResNets, He et al. 2016), there are now many different architectures depending on the targeted task. For segmentation, one of the most promising neural networks is the UNet, which was introduced for medical segmentation (Ronneberger et al. 2015). Many extensions exist, for instance, UNet++ (Zhou et al. 2019) with layers to encode the concatenations, VNet (Milletari et al. 2016), which is dedicated to 3D data, WNet (Xia & Kulis 2017), which has a double UNet architecture, and Attention-UNet (Oktay et al. 2018), which combines UNet with attention layers (Goodfellow et al. 2016). Still, the UNet based architecture remains one of the most effective methods for automatic segmentation.

In the context of astrophysical study, these neural networks have been successfully used in different contexts. For example, Bekki (2021) used the UNet to segment the spiral arms of galaxies. Bianco et al. (2021) used a UNet based neural network called SegUNet to identify H II regions during reionization in 21 cm. Another variant based on UNet and inception neural networks was used to predict localized primordial star formation

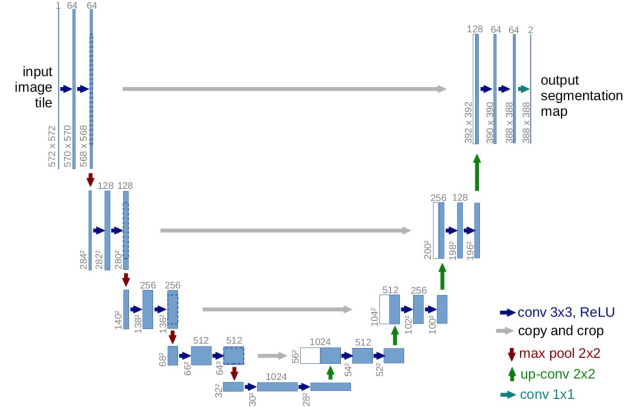


Fig. 7. Illustration of the UNet5 from Ronneberger et al. (2015).

(Wells & Norman 2021). UNet was also used to segment cosmological filaments (Aragon-Calvo 2019). We recommend Hausen & Robertson (2020) for a good introduction to deep learning applied to astrophysical data.

UNet is a multiscale neural network based on convolutional and pooling layers, as presented in Fig. 7. In addition to its simple structure, the strength of this network is an encoder-decoder-based architecture with skip connections. First, the encoder extracts features from the input image down to a coarse scale by using filters and max-pooling. Then, the decoder takes the coefficients at the coarse level and combines them with those from each layer of the encoder via the skip connections, in order to re-inject the details that were lost in the down-sampling (max-pool) step and thereby build a better semantic segmentation map. The final activation function of the network is done by the sigmoid function (Goodfellow et al. 2016), as we wish to have values in order to resolve a segmentation issue,

$$s(x) = \frac{\exp(x)}{\exp(x) + 1}. \quad (1)$$

This function guarantees an output between 0 and 1. Thus, the output of the network can be read as a probability map for the class 1 filament (see Goodfellow et al. 2016, Sect. 6.2.2.2). However, in our case, both the nonequilibrium between the two classes (filament and background) and the incomplete ground-truth prevent the direct interpretation of the segmented map values as probabilities (see Kull et al. 2017, about sigmoid output and probabilities). In the following, we name the intensity value of the segmented maps “classification value”. In this study, the quality of the results is assessed by comparing these classification thresholds with a given threshold (see Sect. 3.1.5). This multiscale mirror-like structure makes the UNet very suitable for image processing such as denoising (Batson & Royer 2019) or segmentation (Ronneberger et al. 2015). Moreover, UNet belongs to the family of fully convolutional networks. These networks are almost independent of the size of the input images (Long et al. 2015). In UNet, the size of the output image will be the same as that of the input if the input is large enough (the minimum size is 32×32 pixels).

A recent and more powerful extension of the UNet model, UNet++, was proposed in (Zhou et al. 2019). This network belongs also to the fully convolutional networks. As illustrated in Fig. 8, the plain skip connections of UNet are replaced with a series of nested dense skip pathways in the UNet++ neural network. The new design aims at reducing the semantic gap between the feature maps of the encoder and decoder sub-networks that

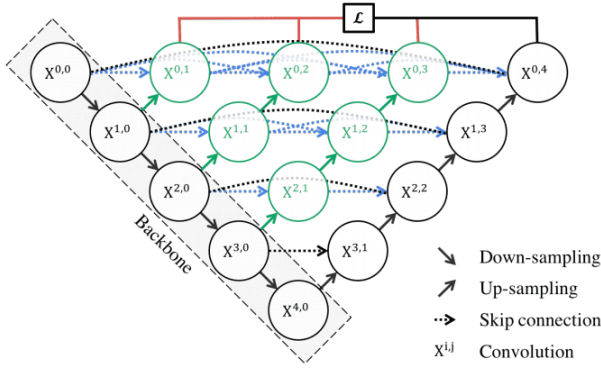


Fig. 8. Illustration of UNet++ from Zhou et al. (2019). The $X^{i,j}$ are the same convolutional layers as for UNet. The difference between UNet and UNet++ can be depicted in three main points: 1) convolution layers on skip pathways (in green), which reduces the semantic gap between encoder and decoder feature maps; 2) dense skip connections on skip pathways (in blue), which improves the gradient flow; and 3) deep supervision (in red), which enables model pruning (Lee et al. 2015).

makes the learning task easier to solve for the optimizer. In fact, the model captures more efficiently fine-grained details when high-resolution feature maps from the encoder are gradually enriched before fusion with the corresponding semantically rich feature maps from the decoder. Note that these “inner” layers have also a mirror-like structure allowing a larger multi-scale representation. However, it is worthy to note that UNet++ requires more data than UNet as the latter has less parameters to tune (see Table 3 in Zhou et al. 2019).

3.1.2. Local normalization

Neural networks such as UNet are highly sensitive to the contrast inside the input images (or patches). This sensitivity comes from the filters that belong to the different convolution layers. In order to avoid this issue, input data are usually normalized, generally by performing a global min-max normalization (Goodfellow et al. 2016). This normalization allows us to temper the dynamic of the contrast while keeping useful physical information about the structures (morphology and gradient). However, in our case, the intensity of the N_{H_2} map presents a very high dynamical range, and a global normalization would artificially weaken many filamentary structures. To avoid this issue, we performed a *local* min-max normalization on each patch. As shown in Fig. 9, this normalization helps to deal with high-contrast variation in nearby regions of the image. However, while this approach solves this issue, the contrast still has high local variations in some cases, so that two nearby patches may show different normalization.

3.1.3. Training with UNet and UNet++

Training a neural network requires a loss function that computes the errors between the model and the ground truth. For segmentation, a recommended function is the binary cross-entropy (BCE), which casts the problem as a classification problem (Jadon 2020). For the sake of clarity, we introduce some notations before we give the expression of the loss function. Let $\{x_i\}_i$ be the set of normalized N_{H_2} patches. Let $\{y_i\}_i$ be the set of segmentation target, that is, the set of binary patches with 1 for filaments pixels and 0 for background pixels. Let $\{m_i\}_i$ be the set of missing data patches, that is, the set of binary patches with 0 for missing pixels and 1 elsewhere. For a given value of i , x_i , y_i ,

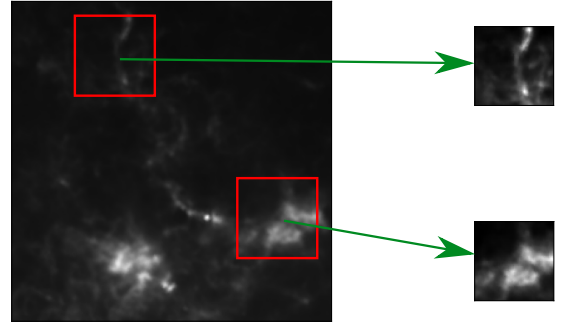


Fig. 9. The *local* min-max normalization of the patches helps to avoid contrast issue allowing a better definition of the filaments.

and m_i share the same Galactic coordinates. The cross-entropy loss for a set of n patches is given by

$$\mathcal{L}(\{x_i, y_i, m_i\}_i; \theta) = \frac{1}{np^2} \sum_{i=1}^n \sum_{k,l=1}^p m_i[k, l] (y_i[k, l] \log(f_\theta(x_i)[k, l]) + (1 - y_i[k, l]) \log(1 - f_\theta(x_i)[k, l])), \quad (2)$$

where f_θ is the function that applies the forward propagation, and θ are the weights of the neural network. By using $\{m_i\}_{i \in [1..n]}$, we ensure that only labeled data are used.

As we have many unlabeled pixels in the patches (see Sect. 2.2), we have to adapt the training step to avoid inconsistencies. We summarize the different steps in Fig. 10. First, in step (1), we take a set of patches (a batch) and then apply the augmentation process (step (2)) on these patches. During this step (2), we ensure that for a given i , the same transformation is applied on x_i , y_i , and m_i . The following steps are about computing the prediction errors of the model on the patches and making the back-propagation of the gradient of these errors in order to update the weights of the neural networks (Goodfellow et al. 2016). Therefore, in step (3), we begin to apply the network f_θ on the patches (forward propagation). Since this step implies using the convolution layers in the network, we use both unlabeled and labeled pixels. This is important as the neural network needs the neighboring pixels to compute the value for one pixel. After we restrict the result (step (4)) to labeled and nonmissing pixels using the mask m_i , we can compute (step (5)) the errors on the restricted results compared to the ground truth. Finally, in step (6), we update the weight of the network using the back-propagation of the gradients of the errors. This is done by using a stochastic gradient descent scheme (Goodfellow et al. 2016) with a learning rate μ_i that changes during the training step following the epochs.

3.1.4. Building the segmentation map

When the neural network has been trained, we can apply the model to segment an image. As we described before, during the creation of the data set (Sect. 2.2), we must deal with the high dynamic contrast in images. Again we propose to solve the issue by taking small patches and apply a local min-max normalization. Moreover, since two closed patches may have a different contrast, the normalization can lead to variation in the results when applying the neural network. Therefore, in order to resolve this issue, we propose to use an overlapping sliding window to obtain the patches: the segmentation result is then the average

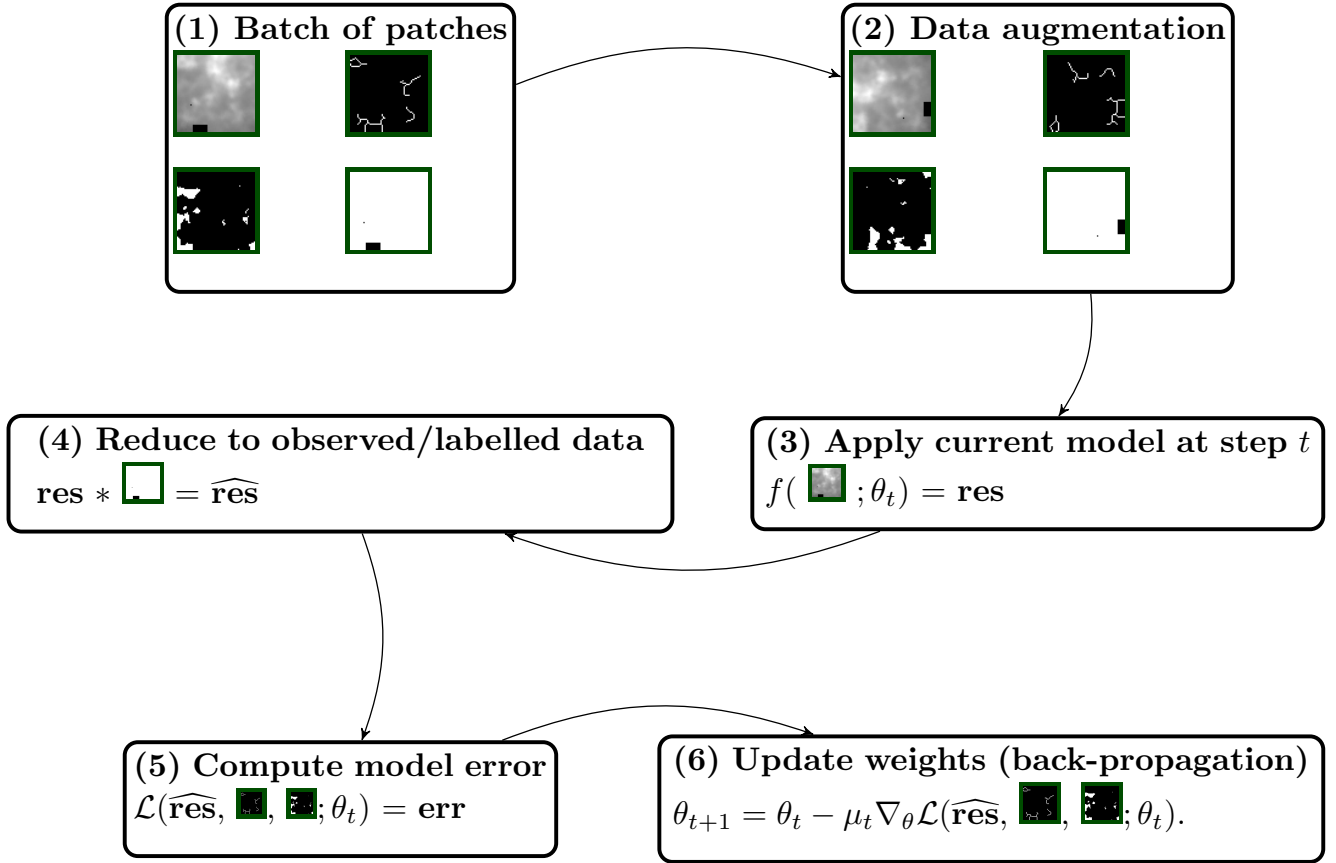


Fig. 10. Five steps of an epoch during the training. For illustration purposes, we reduced the batch to a set of one patch. θ_t represents the weights of the neural network at epoch t , and μ_t is the learning rate at epoch t .

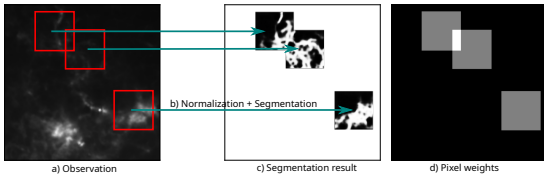


Fig. 11. Segmentation process. It takes patches from an observation (a), then normalizes the patch and applies the segmentation model (b), the segmented patch is positioned at the same coordinates (c), and is finally weighted by coefficients (d) representing the number of patches in which each pixel appears. Because a sliding window with overlap is used, a given pixel is segmented several times (as long as it falls in the sliding window). Then, we obtain several segmentation values for the same pixel. The final segmentation value assigned to the pixel corresponds to the average of all the segmentation values computed from the contributing sliding windows.

between the output of the neural network applied on the patches. These patches are distinct from those used for learning the network (see Sect. 2.2). As the variance of contrast between patches introduced variance inside the output results of the neural network, the overlap and averaging operation (see Fig. 11) allows us to decrease the artifact that may appear (Pielawski & Wählby 2020).

Thus, we apply the following segmentation procedure (illustrated in Fig. 11). We browse the image using an overlapping sliding window that gives patches (step (a)). Each patch is then normalized using a min-max normalization (step (b)); here we avoid the missing data (around borders and saturated areas).

Table 1. Confusion matrix.

		Predicted	
		Filament	Background
Actual	Filament	TP	FN
	Background	FP	TN

Then, we apply the trained neural network on the patch to obtain the density map output and add on the output image at the coordinate of the patches (step (c)). Since we use an overlapping sliding window, the results are added to the output, and then we divide each pixel by a weight representing the number of patches in which the pixel appears (this is done using the weight map built in step (d)).

3.1.5. Metrics

In supervised classification problems, the confusion matrix, also called error matrix, is computed in order to assess the performance of the algorithm. We refer to the filament and background classes as the positive (P) and the negative (N) classes, respectively. We also refer to the correctly and misclassified pixels as true (T) and false (F), respectively. In a binary classification problem, the confusion matrix is thus expressed as in Table 1.

The confusion matrix is evaluated on the estimated filament masks that are deduced from the segmented map at a

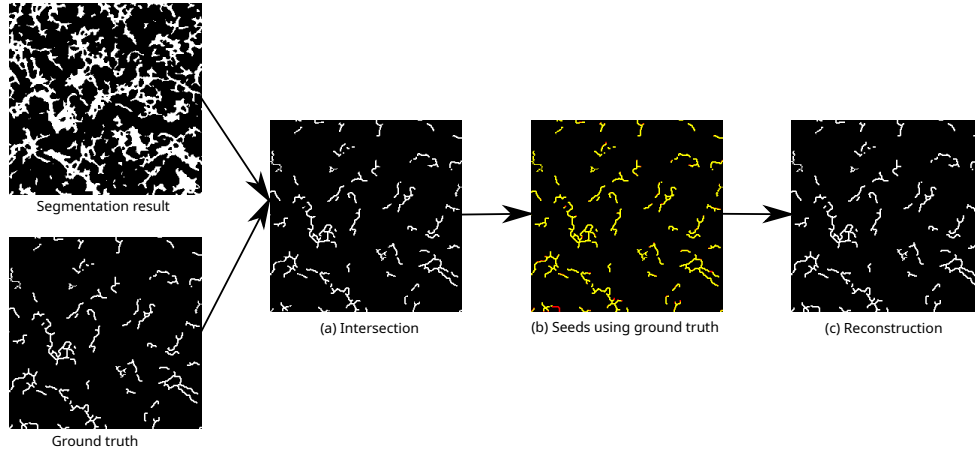


Fig. 12. Morphological reconstruction is a method that computes shapes from marked pixels called seeds. (a) We first compute the seeds using the intersection between the segmentation results and the ground truth. (b) We use the intersection pixels as seeds (see the red seeds in the bottom left corner). (c) We apply the reconstruction to obtain the filaments with at least one seed.

classification threshold. It is important to recall, however, that the evaluation set is restricted to labeled data. The classification scores are thereafter derived from the confusion matrix. In this work, the recall, precision, and dice index defined in Eqs. (3), (4) and (5), respectively, are used to evaluate the classifier performance. Maximizing recall and precision amounts to minimizing false-negative and false-positive errors, respectively, whereas maximizing the dice index amounts to finding the optimal tradeoff between the two errors. Therefore, the closer to 1 these scores, the better.

$$\text{Recall} = \frac{TP}{TP + FN} \quad (3)$$

$$\text{Precision} = \frac{TP}{TP + FP} \quad (4)$$

$$\text{Dice} = \frac{2 TP}{2 TP + FP + FN} \quad (5)$$

In addition to the recovery scores, we also calculate the rate of missed structures (MS) in segmentation for the same set of thresholds. The MS score can be defined as the ratio of the missed filament structures over all the input filament structures,

$$\text{MS} = \frac{\text{Number of missed structures}}{\text{Total number of filament structures}} \quad (6)$$

The MS metric is based on morphological reconstruction (Vincent 1993; Soille 2003; Robinson & Whelan 2004). Figure 12 shows how we apply this method to assess which known filaments are recovered. First, we compute the intersection between the known filaments (ground truth) and the segmentation results (Fig. 12a). Then we use this intersection as the seed for the reconstruction method: in Fig. 12b, the yellow elements are the seeds, and the red elements are the part of filaments that is missed. The morphological reconstruction takes the seeds to recover the known filaments by using a shape-constrained growing process (Fig. 12c). Only the filaments for which at least one pixel is used as seed will be recovered (Robinson & Whelan 2004). By subtracting the morphological reconstruction result from the ground truth, we can identify the missed structures (see also Fig. 17). Then we count the number of missed structures by using a direct labeling of the pixels where two neighboring pixels share the same label

Table 2. Experimental setup.

Parameter	Value
Patch size (p)	32 pixels
Dataset split	{80%, 10%, 10%}
Batch size	64 patches
Epochs	100
Initial learning rate	{ 10^{-5} , 10^{-4} , 10^{-3} , 10^{-2} }

Notes. Parameters used in the experimental setup for UNet and UNet++ training

(Fiorio & Gustedt 1996). Then, we can compute the MS metric and qualitatively assess the recovery of filaments in terms of structures, rather than individual pixels.

3.2. Experimental setup

Taking the analysis of the normalization in Sect. 2.2 into consideration, the patch size was fixed to the lowest value accepted by the UNet family, $p = 32$. In order to have proper training, validation, and test steps, we randomly split our initial set of patches (Sect. 2.2) into three sets, namely, the training, validation, and test sets, with proportions of 80%, 10%, and 10%, respectively. The random split ensures the presence of the two classes (filament and background) in the three sets. The patches in training and validation sets were then shuffled after each epoch to help avoiding unwanted bias (see, Goodfellow et al. 2016). The total number of epochs was set to 100. UNet and UNet++ were trained using the Adam optimization scheme with a multistep learning rate (Kingma & Ba 2015; Ronneberger et al. 2015). During the first 30 epochs, the initial learning rate value was divided by 10 every five epochs. Four initial values of the learning rate, 10^{-5} , 10^{-4} , 10^{-3} , and 10^{-2} , were tested for both networks. We denote by UNet[lr] (UNet++[lr]) the UNet (UNet++) model learned with lr as the initial value of the learning rate, where $lr \in \{10^{-5}, 10^{-4}, 10^{-3}, 10^{-2}\}$. A summary of the parameter values used in the training step is given in Table 2. In the segmentation step, an overlapping sliding window of size 32×32 was applied, where an overlap of 30 pixels was used in order to limit edge artifacts and to generate highly smooth segmentation.

In order to compare the performance of UNet with UNet++, two zones of the global N_{H_2} mosaic were excluded from the initial patch data set. Constrained by the limited number of patches in the data set, small zones were removed, namely, the zones $166.1\text{--}168.3^\circ$ and $350.3\text{--}353.5^\circ$. The choice of the removed regions was motivated by assessing the network performance in regions with a highly diverse column density and filaments content. While $350.3\text{--}353.5^\circ$, removed from mosaic $349\text{--}356^\circ$, is dense and rich in filaments (38541 filament pixels), the region $166.1\text{--}168.3^\circ$, removed from the mosaic $160\text{--}171^\circ$, is sparser and contains fewer filaments (1459 filament pixels). The filament density is always inferred based only on the incomplete ground truth (labeled part of the data set). The two removed zones were then segmented by the learned models, and the segmentation quality was assessed using the evaluation scores described in Sect. 3.1.5. The evaluation scores were also computed on the fully segmented Galactic plane in order to have a global performance evaluation of models.

4. Results

4.1. Scores and segmented mosaic analysis

In order to evaluate the training performances, we discuss below the different scores we obtained for the different tested scenarios. Two neural networks were tested (UNet and UNet++) with four different initial learning rates for each. For an input column density image, the segmentation process (see Sect. 3.1.4) returns a classification value mask from which it is possible to identify pixels that likely belong to a filamentary structure. Nevertheless, we did not attempt to extract the filaments like Schisano et al. (2020) did. We postpone this physical analysis on the newly identified filaments to a follow-up work. Here we present the method as a proof-of-concept and analyze its performances and returned results (segmented map of the whole Galactic plane). We illustrate these results on two portions of the Galactic plane that were selected for their characteristics in terms of column density and filament content (as known from the input data set of filament mask based on the spine+branches).

To evaluate the performances of the different scenarios, Fig. 14 presents the BCE curves for the training set and the validation set during the first 30 epochs. For all models, these loss curves reach a plateau around the tenth epoch, confirming the rapid convergence of UNet-based networks. The performance of UNet++[10^{-2}] was removed from the displayed results due to convergence issues. As shown in Fig. 14 and confirmed by this analysis, the models have similar performances and converge to a training error around 0.01, except for schemes with a starting learning-rate value of 10^{-5} , where higher errors are reported (more than 0.016 and 0.012 for UNet[10^{-5}] and UNet++[10^{-5}], respectively). The similar performances obtained for the two architectures and the different learning rates indicate that the method is robust. Validation errors are slightly higher than training errors, with a difference up to 0.0011, except for UNet[10^{-5}] (around 0.002) and UNet++[10^{-5}] (around 0.0018). The reported values indicate that the learned models show low bias and low variance.

For both UNet and UNet++, the best performance is with an initial learning-rate value of 10^{-3} . Overall, the best model in terms of loss function is the UNet++[10^{-3}]. For each scenario, the best-performing model in validation was used to segment the test set and compute the underlying BCE (see Table 3). BCEs calculated on the test set corroborate the previous analysis: scenarios with initial learning rates in [10^{-2} , 10^{-3} , 10^{-4}] result in

similar test errors that do not exceed 0.009, whereas scenarios with initial learning rates of 10^{-5} show a higher error. The lowest test error corresponds to the scenario UNet++[10^{-3}].

In Fig. 13 the dice index curves for the training and validation sets is plotted for different classification thresholds. The dice index was also computed on a test set using the best-performing models in validation (the models used in Table 3), and the corresponding results are given in Fig. B.1. In the same way, the dice index results are in line with the BCE. These models were used afterwards to segment the removed zones $166.1\text{--}168.3^\circ$ and $350.3\text{--}353.5^\circ$. Figure 16 presents the results of the segmentation process for the different scenarios tested and presented in Table 2. All segmented maps are presented within the range [0, 1]. Overall, the obtained images are in line with the analyzed BCEs. The scenarios with initial learning rates of 10^{-2} , 10^{-3} , and 10^{-4} return very similar segmented maps. A noticeable difference is seen in maps that were segmented by both UNet and UNet++ with an initial learning rate of 10^{-5} . In these cases, the filamentary structures are broader than those obtained for the other scenarios, especially for UNet. Moreover, the intensity of the segmentation maps also varies for these last two scenarios, where the low-value structures are better revealed (intensity variation up to a factor of 10 in those zones). The ability of these two last scenarios (and of the UNet in particular) to better reveal structures with a lower classification threshold might be used to detect structures that are not well seen on the original map, either due to their low contrast and/or their low column density. A close visual inspection of the column density images confirms that features revealed by UNet[10^{-5}] and UNet++[10^{-5}] are low-contrast filaments that were present in the original images, but absent from our input catalog of filaments that was used as ground truth.

In Fig. 15, precision–recall curves (P–R curves) are shown for $350.3\text{--}353.5^\circ$ (top left) and $166.1\text{--}168.3^\circ$ (top right). The P–R curve represents precision vs recall for different threshold values. It is used to estimate the optimal threshold that maximizes the dice index (a trade-off between precision and recall). The more the P–R curve tends to the (1, 1) corner, the better the model. In other terms, the larger the area under the curve, the better the model. The objective is to estimate the optimal threshold that returns a trade-off between precision and recall. For clarity sake, all curves are zoomed in from 0–1 to 0.7–1 for precision and recall. In all figures, black asterisks refer to the precision–recall values at the optimal threshold; the values of the latter are reported in Tables 4, 5, and B.2. Different approaches can be used to compute the optimal threshold, such as minimizing the difference between the precision and recall, or minimizing the Euclidean distance between the P–R curve and the optimal performance, corresponding to a precision–recall of (1, 1). Here, we computed the optimal threshold as the one that maximized the dice index (trade-off between filament and background recovery). In Tables 4 and 5, we report four samples from these P–R curves corresponding to conservative (0.8), medium (0.5), relaxed (0.2) and optimal (giving the best Dice index) thresholds. When investigating the dense zone of $350.3\text{--}353.5^\circ$, we note that, for a given threshold, all the models give results with similar performances (Dice indices $>85\%$), except for UNet[10^{-5}] (74.79% at threshold 0.2). Close optimal threshold are also obtained for all models, where values are situated between 0.35 and 0.48. Note that at the conservative threshold 0.8, UNet[10^{-5}] and UNet++[10^{-5}] result in low recall values compared with the remaining scenarios (72.96% and 75.14%, respectively), confirming the results reported with the segmented map where salient filaments are detected with lower values in these two scenarios compared with the remaining ones. However, they tend

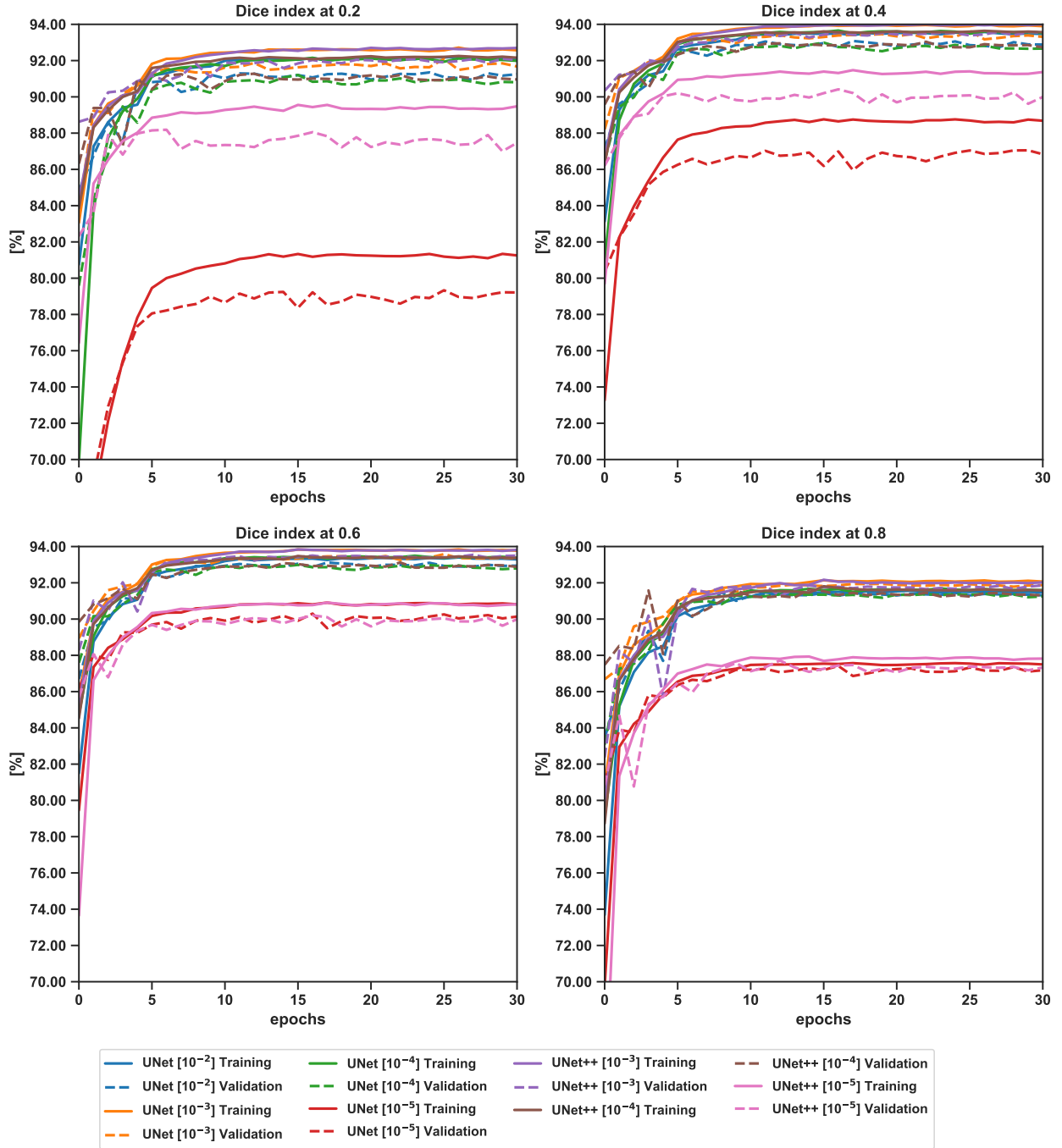


Fig. 13. Dice curve evolution of schemes reported in Fig. 14 are displayed over the first 30 epochs in training (continued lines) and validation (dashed lines) steps, at classification threshold values 0.8, 0.6, 0.4, and 0.2. The displayed curves are aligned with the results deduced from BCE curves, where close performances were obtained with initial learning-rate values of 10^{-4} , 10^{-3} , and 10^{-2} , and a poorer performance is obtained for schemes with a learning-rate value of 10^{-5} . The highest dice score is reported for UNet++ [10^{-3}] (purple), and the lowest performance corresponds to the UNet [10^{-5}] scheme, (red) especially at thresholds 0.2 and 0.4. Similar to the BCE curves and for all displayed schemes, a plateau regime is reached within the first ten epochs.

to be more performing when decreasing classification threshold, especially at threshold 0.2 where they are performing better than the remaining scenarios (the best recall is of 98.1% with UNet [10^{-5}], followed by UNet++ [10^{-5}] with a recall value of 97.26%). This can be explained by the low value structures that are better revealed in these two scenarios as noticed before in the segmented map. In Table B.2, precision, recall and Dice index are computed on the fully-segmented Galactic plane, to infer the global segmentation performance. The resulting global scores

are inline with the ones obtained with the dense zone where, for a given threshold, all models show close performances, except UNet [10^{-5}] and UNet++ [10^{-5}] slightly less performing. Moreover, the optimal thresholds obtained with the global segmentation are close to thresholds obtained for the dense mosaic, where values range from 0.3 to 0.44. This result suggests that either the training step is more driven by high density regions and/or that these regions better represent the global properties observed on the Galactic plane.

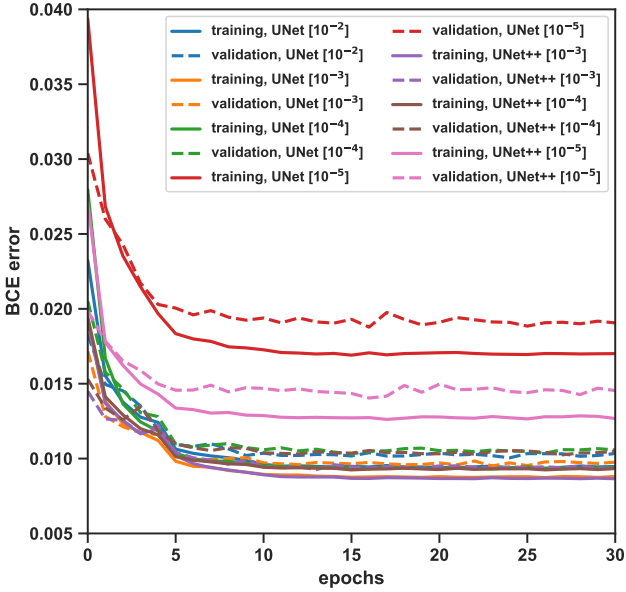


Fig. 14. BCE evolution over the first 30 epochs in training (continued lines) and validation (dashed lines) steps. UNet++[10^{-2}] schemes is removed as its corresponding BCE diverged. The displayed schemes show similar performances. Models with a learning-rate value of 10^{-5} resulted in higher BCEs. The lowest error is reported for UNet++[10^{-3}] (purple), and the highest error corresponds to the UNet[10^{-5}] scheme (red). A plateau regime is reached within the first ten epochs for all models, which confirms the rapid convergence of the UNet-based networks.

Table 3. Binary cross entropy.

Model	BCE Score
UNet[10^{-2}]	0.0085
UNet[10^{-3}]	0.0084
UNet[10^{-4}]	0.0088
UNet[10^{-5}]	0.0161
UNet++[10^{-3}]	0.0081
UNet++[10^{-4}]	0.0088
UNet++[10^{-5}]	0.0122

Notes. Binary cross entropy (BCE) evaluation on the test set for the schemes reported in Fig. 14. The lowest (highest) achieved BCE is given in blue (red). BCE values in test are inline with performances in training and validation steps with UNet++[10^{-3}] and UNet[10^{-5}] resulting in the best and less performing schemes, respectively.

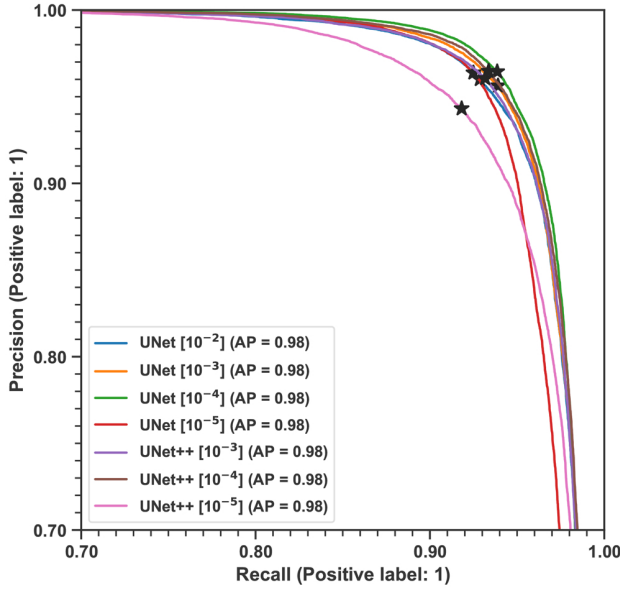
When examining the scores of the sparse zone of 166.1° – 168.3° in Table 5, all the models result in similar performances in precision. However, the recall performance per threshold has a higher contrast, where UNet++[10^{-5}] shows lower recall values for thresholds 0.8, 0.5, and 0.2. While the background is well recovered (the lowest precision is of 98.97%), lower recall values are obtained compared to the dense zone, where we had to relax the threshold to 0.2 in order to improve filament recovery and obtain recall values higher than 70%. Similarly to the dense zone, close optimal dice indices were obtained for all models, where the difference between the best dice given by UNet++[10^{-4}] (99.38%) and the more poorly performing UNet[10^{-2}] (98.8%) is less than 0.6%. Although interesting scores are obtained at the optimal thresholds, it is very important to underline the very low values of these thresholds in all

scenarios. Optimal thresholds range from 0.01 to <0.03 , except for UNet[10^{-5}] (0.12). The obtained values reflect the difficulty of the different networks to reveal structures in this mosaic, where almost 40% to 60% of the filament pixels are detected with classification values lower than 0.5 (see the segmented maps in Fig. 16). Moreover, we clearly note the discrepancy between scores computed on the sparse zone and the global scores reported in Table B.2, which might suggest that the trained models are more successful in revealing filaments in dense than in lower density zones. It is difficult, however, to conclude about the origin of this discrepancy because the number of labeled pixels (in both filament and background) is very different between the sparse and the dense zone. Limited labels in the sparse mosaic also imply that the computed scores with higher uncertainties need to be considered. Nevertheless, visual inspection of the segmented maps in Fig. 16 results in similar trends as observed for the dense zone, where close performances are noted for all models except for the models with an initial learning rate of 10^{-5} . These models reveal more details at moderate to low classification values.

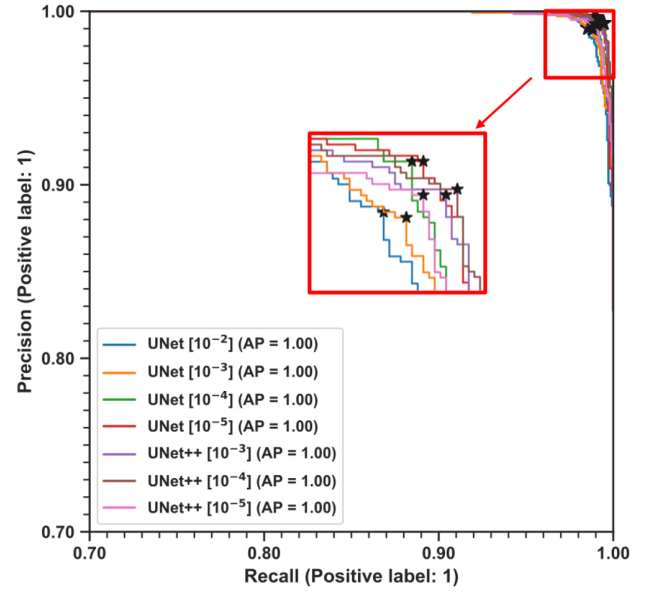
4.2. Analysis of missed structures

In addition to pixel-level scores, the structure-level score was also computed in order to evaluate filament recovery in terms of structures. When some pixels of a given filament are missed, it does not automatically imply that the whole structure is missed. In Tables 4 and 5, the MS rate is computed at different classification thresholds for dense and sparse zones. As expected, the higher the threshold, the more structures are missed. Overall, we note that at conservative (0.8) and moderate (0.5) thresholds, low MS rates are obtained for dense mosaics compared with the sparse mosaic. In the latter, more strongly contrasting values are obtained across the classification thresholds where MS rates range from 0 (all structures are revealed) to almost 60% (more than half of the structures are missed; see the MS rates in Table 5). In a region with a low concentration of filaments, missing (or detecting) a structure would have more impact on the MS rate variation than in a dense region. Similarly to pixel-level scores, the global MS rates reported in Table B.2 are closer to the values obtained with the dense zone than the sparse zone, and this for the same reasons as we invoked for pixel-level scores.

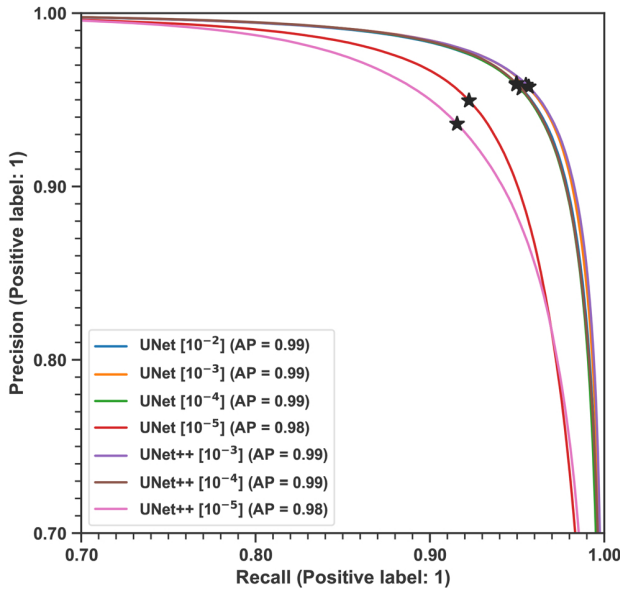
In order to learn more about the structure of missed filaments, a missed-structure map at a classification threshold of 0.8 was built. In this map, any structure that was missed by any model is represented. Here, the map intensity encodes the number of models that missed the structure, so that values range from 0 (detected structure) to 7 models (missed by all models). In Fig. 17, representative portions from the sparse and dense regions are displayed. We note the prevalence of structures that were missed by all the models (yellow). In fact, 50% of the missed structures in the whole Galactic plane are the same for all the models. After a close visual inspection of the missed structures, two categories are reported. The first category consists of small structures, which is the most prevalent category. These structures either correspond to small isolated filaments and/or to small parts that are missed in larger filaments. The second category corresponds to larger filaments that are misidentified as filaments in the ground truth. For example, structures reported in Fig. 17 (bottom right) at positions $(349^{\circ}, 1^{\circ})$ and $(350.5^{\circ}, -1^{\circ})$ are excluded from the filament class. There are also isolated square-shaped structures that are mislabeled as filaments in the ground truth, corresponding to saturated pixels (see Fig. 17 (bottom right) at position $(350.8^{\circ}, 1^{\circ})$). Unfortunately,



(a) PR curves for 350.3–353.5°



(b) PR curves for 166.1–168.3°



(c) PR curves for the fully segmented Galactic plane

Fig. 15. P–R curves of the schemes reported in Fig. 14, computed on the segmented removed zones (top) and the full Galactic plane (bottom). (a) P–R curves computed on the segmented 350.3–353.5°, which corresponds to the dense region that was removed from the patches data set. (b) P–R curves computed on the segmented 166.1–168.3°, which corresponds to the sparse region that we removed from the patches data set. (c) P–R curves computed on the full segmented Galactic plane. Unlike in Fig. 15b, P–R curves obtained on the latter are close to those obtained in Fig. 15a.

trained models fail to reject these saturation bins when they are entangled within a true large filamentary structure.

4.3. New possible filaments revealed by deep learning

Based on the performance analysis in Sect. 4.1, two groups of models can be derived based on the initial learning rate: (1) models with an initial learning rate of 10^{-4} , 10^{-3} , and 10^{-2} , and (2) models with an initial learning rate of 10^{-5} . In the following, we present the segmentation results that we illustrate for the best model, UNet++[10^{-3}], on the two selected submosaics.

Figure 18 presents the evolution of the segmented map for the two selected regions as a function of the segmented map threshold.

In both regions, more pixels are classified as filaments by the training and segmentation processes than in the input structures (input filament mask used as the ground truth in the supervised training). The ratio (new filament pixels to input filament pixels) varies between 2 and 7, depending on the threshold value (from 0.8 to 0.3, the optimal threshold). The same conclusions are drawn for the whole Galactic plane. In Fig. 19, the distribution of candidate filament pixels across the entire Galactic plane,

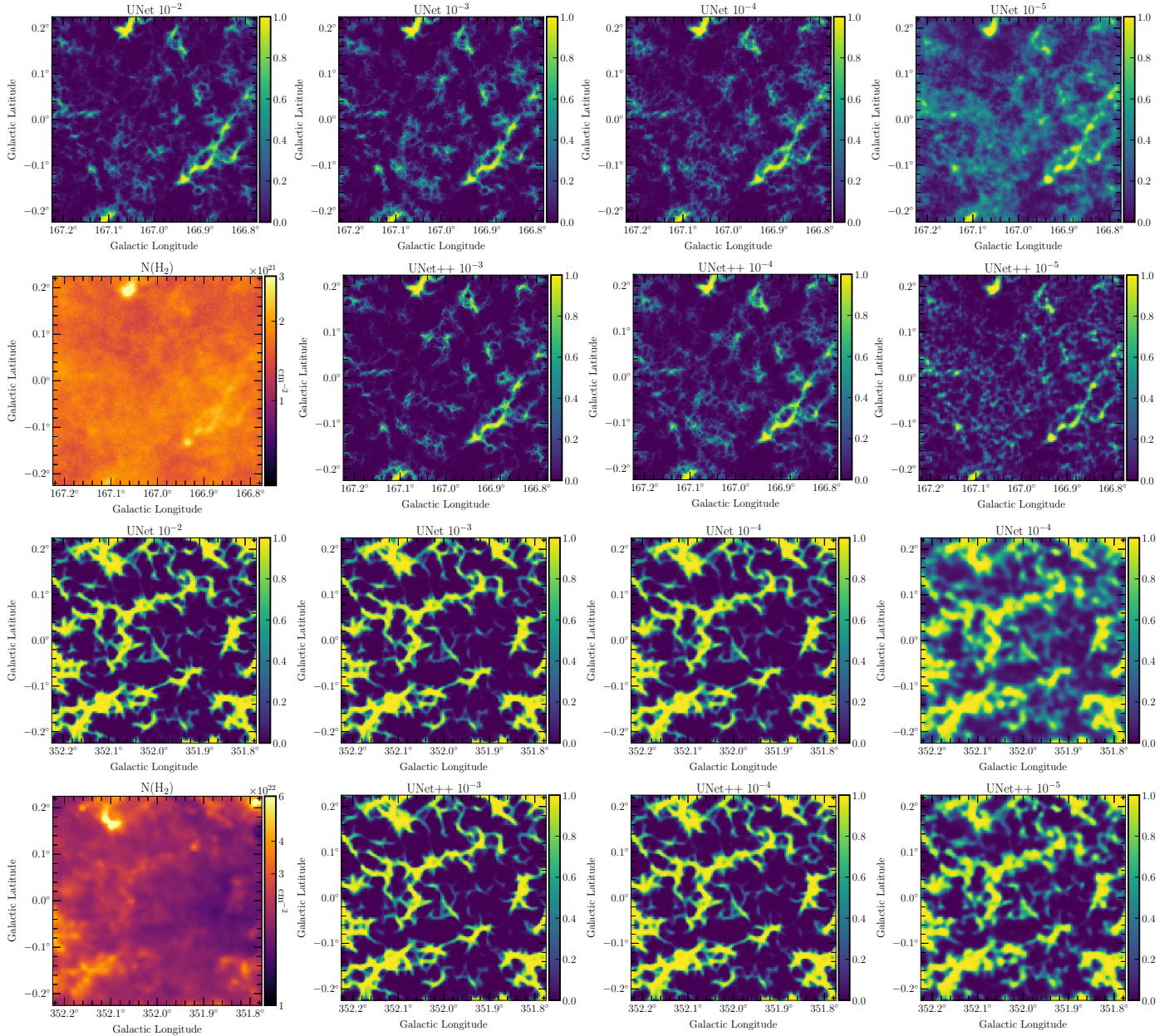


Fig. 16. Segmented maps obtained for the models analyzed in Fig. 14, zooming in on a part of the two regions that was removed from the training namely, the $l = 166.1\text{--}168.3^\circ$ (top) and $l = 350.3\text{--}353.5^\circ$ (bottom; see the red zones identified in Fig. 3). The segmented images are displayed in the range $[0, 1]$ representing the classification value according to which a pixel belongs to the filament class. For each region, the first row shows results of the UNet segmentation, and the second row shows results of the UNet++ segmentation with initial learning-rate values of 10^3 (left), 10^{-4} to 10^{-5} (right). The UNet++ with a learning rate of 10^{-2} is not presented because of diverging results (see Sect. 4.1). The N_{H_2} is shown at this position for each region. The regions are $0.45^\circ \times 0.45^\circ$ wide.

estimated in bins of $4.8^\circ \times 0.16^\circ$, is displayed for the ground truth and the segmentation results at different classification thresholds. Even at a conservative classification threshold of 0.8, more pixels are labeled as filaments than in the ground truth used in the learning step. As expected, the more we decrease the classification threshold, the more pixels are labeled as filament. A close visual inspection of the segmented images indicates that structures observed at thresholds lower than the optimal value are also seen on the original column density image, but were not previously detected due to their low contrast with respect to the surrounding background emission. The squared structures shown in Fig. 18 (bottom) are saturated pixels corresponding to bright sources located in filaments. These structures also appear in the

ground truth, and we therefore retrieve them when applying our model. Because we lack information about the column density in these saturated pixels, we left them as squares in the segmented maps.

Figure 20 presents the same result as Fig. 18, but for the binarized version of the segmented map. The filamentary structures identified at a given threshold are now represented as 1 when the associated pixel belongs to the filament class 0 instead. This representation allows a more direct comparison with the input filament mask (spine plus branches; see Fig. 2). However, the classification value itself (that indicates whether a pixel belongs to the filament class) no longer appears in this representation. As for results presented in Fig. 18, the threshold decrease has

Table 4. Segmentation scores (350.3–353.5°).

Model Scores (%)	UNet [10 ⁻²]	UNet [10 ⁻³]	UNet [10 ⁻⁴]	UNet [10 ⁻⁵]	UNet++ [10 ⁻³]	UNet++ [10 ⁻⁴]	UNet++ [10 ⁻⁵]
Precision at 0.8	99.67	99.76	99.84	99.89	99.71	99.76	99.65
Precision at 0.5	97.45	98.06	98.24	97.11	97.87	97.87	95.13
Precision at 0.2	88.10	89.75	88.79	60.42	90.12	87.59	78.58
Precision at thr _{opt}	96.01	95.63	96.45	96.38	96.06	96.48	94.32
Recall at 0.8	79.15	79.45	79.10	72.96	78.34	79.71	75.14
Recall at 0.5	91.15	90.86	91.63	91.75	90.45	91.73	90.97
Recall at 0.2	96.55	96.27	96.83	98.10	96.09	96.82	97.24
Recall at thr _{opt}	92.86	93.91	93.86	92.49	93.17	93.37	91.82
Dice at 0.8	88.24	88.45	88.27	84.33	87.74	88.62	85.67
Dice at 0.5	94.19	94.33	94.82	94.35	94.02	94.70	93.00
Dice at 0.2	92.13	92.89	92.64	74.79	93.01	91.98	86.92
Dice _{opt}	94.41	94.76	95.14	94.40	94.59	94.90	93.05
MS at 0.8	4.25	4.96	4.96	7.79	4.96	5.31	6.02
MS at 0.5	1.06	1.24	1.24	1.42	1.59	1.42	1.06
MS at 0.2	0.35	0.18	0.35	0.18	0.35	0.18	0.18
MS at thr _{opt}	0.53	0.35	0.53	1.24	0.53	0.53	0.88
thr _{opt}	0.41	0.35	0.38	0.48	0.37	0.42	0.47

Notes. Segmentation scores evaluated on the dense zone of 350.3–353.5° segmented by the models reported in Fig. 14. Precision, recall, dice index, and MS rate are evaluated at classification threshold values of 0.8, 0.5, 0.2, and the optimal threshold. The latter refers to the threshold value optimizing the dice index and estimated using P-R curves (see Fig. 15a). Blue (red) refers to the best (least performing) model in each row. The bold scores correspond to the absolute best (if in blue) or lowest (if in red) performance per score.

Table 5. Segmentation scores (166.1–168.3°).

Model Scores (%)	UNet [10 ⁻²]	UNet [10 ⁻³]	UNet [10 ⁻⁴]	UNet [10 ⁻⁵]	UNet++ [10 ⁻³]	UNet++ [10 ⁻⁴]	UNet++ [10 ⁻⁵]
Precision at 0.8	100.00	100.00	100.00	100.00	100.00	100.00	100.00
Precision at 0.5	100.00	100.00	100.00	100.00	100.00	100.00	100.00
Precision at 0.2	100.00	100.00	100.00	100.00	100.00	100.00	100.00
Precision at thr _{opt}	99.04	98.97	99.65	99.66	99.25	99.32	99.24
Recall at 0.8	25.91	28.38	25.22	25.29	33.45	30.64	20.84
Recall at 0.5	49.01	58.40	49.01	54.90	63.33	60.59	41.74
Recall at 0.2	77.11	87.32	81.49	94.59	87.18	87.73	72.86
Recall at thr _{opt}	98.56	98.83	98.90	99.04	99.31	99.45	99.04
Dice at 0.8	41.15	44.21	40.28	40.37	50.13	46.90	34.49
Dice at 0.5	65.78	73.73	65.78	70.88	77.55	75.46	58.90
Dice at 0.2	87.07	93.23	89.80	97.22	93.15	93.46	84.30
Dice _{opt}	98.80	98.90	99.28	99.35	99.28	99.38	99.14
MS at 0.8	61.02	45.76	57.63	50.85	32.20	37.29	44.07
MS at 0.5	16.95	6.78	10.17	15.25	6.78	6.78	11.86
MS at 0.2	1.69	0.00	1.69	0.00	0.00	1.69	1.69
MS at thr _{opt}	0.00	0.00	0.00	0.00	0.00	0.00	0.00
thr _{opt}	0.03	0.03	0.02	0.12	0.01	0.02	0.02

Notes. Same as in Table 4, but for the sparse zone of 166.1–168.3°.

two effects: (i) more pixels are identified as belonging to the filament class (new structures are detected, in particular, those with a faint-to-low contrast that are barely visible in the original N_{H_2} image), and (ii) a given structure becomes thicker. This last effect can be identified as a lowering of the corresponding column density threshold, where the highest threshold

identifies the densest part of the filament. It is interesting to note that the optimal threshold (as well as lower threshold values) in both regions identifies the filamentary structures as observed in the original column density map, down to their external envelope emission, before reaching the background emission. This result is important because it will allow a precise study of the

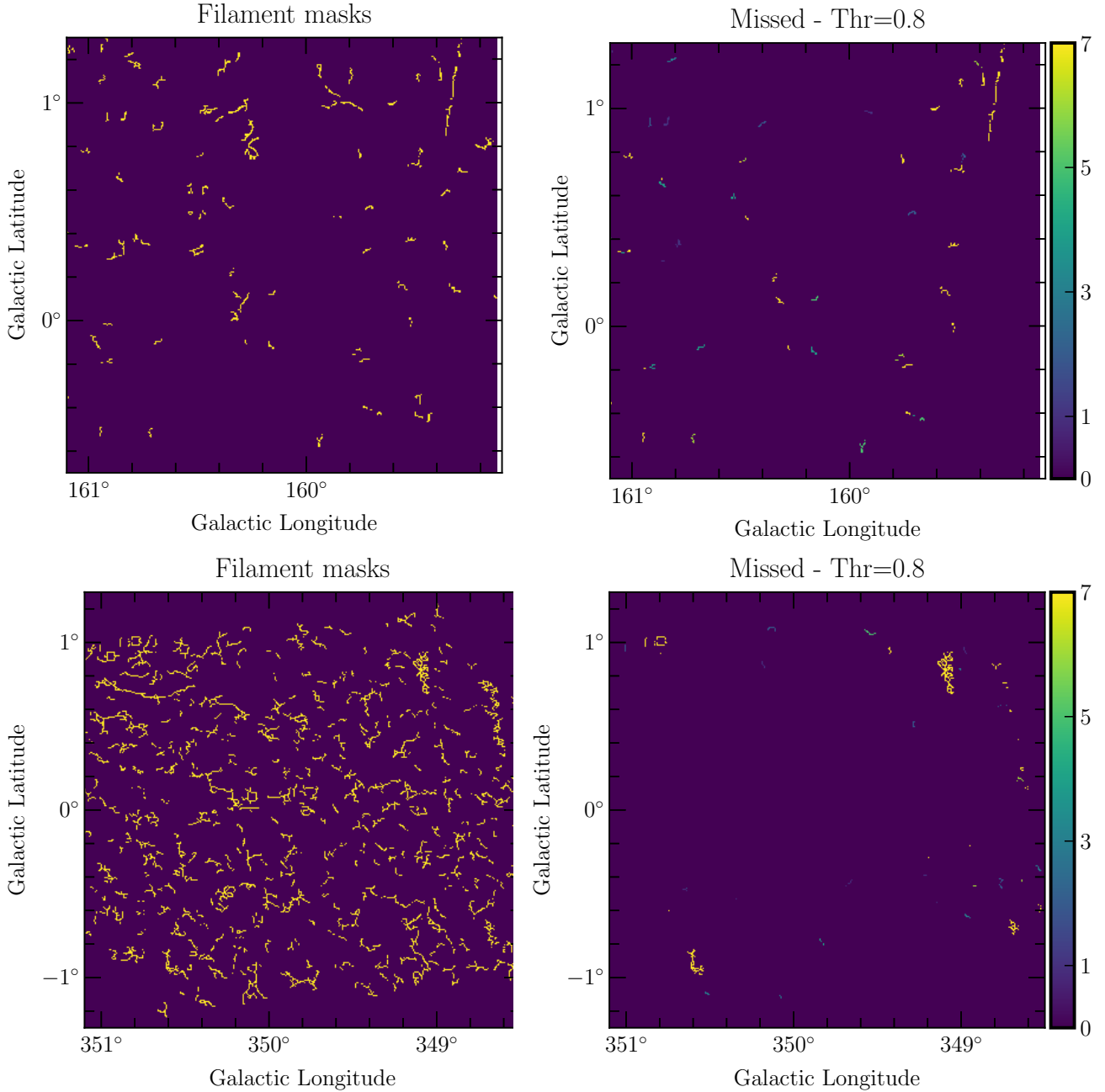


Fig. 17. Input filaments missed by the segmentation process on the $l = 160\text{--}171^\circ$ (top) and $l = 349\text{--}356^\circ$ (bottom) regions of the Galactic plane, respectively. We show. The input filament mask (left) and the missed structures at a classification threshold of 0.8 in a cumulative way (for all the scenarios; right). The unit (color-coding) for the missed structures maps corresponds to the number of tested scenarios (from 1 to 7) that missed a given structure.

filament-background relation. The widening of the filamentary structures can also be seen as the definition of the RoI given by [Schisano et al. \(2020\)](#); see also Fig. 2, bottom right). [Schisano et al. \(2020\)](#) defined the RoI as the objects that define filamentary candidates in their catalog. This point is important because it implies that the comparison of our segmented map results with the RoI would lower the factor we derived that represents the number of pixels classified as filament as the RoI are always thicker than the spine plus branches we used as input in this work to train the network to learn what a filament is. In this work, we infer the filament mask as a ground truth from the filament spine plus branches, as shown on Fig. 2 (bottom left). However, the RoI defines the filament in order to

delineate its spread on the column density map, and this corresponds to the observed widening of the structures with the lowering of the threshold. The comparison of the different structures is illustrated in Fig. 21. Because we used spine plus branches as input to define a filament here, we kept this input structure as a reference to compare with the result of the segmentation process.

A key point in this work is to ascertain the nature of the filamentary structures we reveal. Filaments are made of gas and dust. The filaments detected by [Schisano et al. \(2020\)](#) are traced in dust emission maps. Dust grains emit over a wide range of wavelengths, and they act as absorbers in the optical, near-, and mid-infrared parts of the spectrum. Because of their dusty

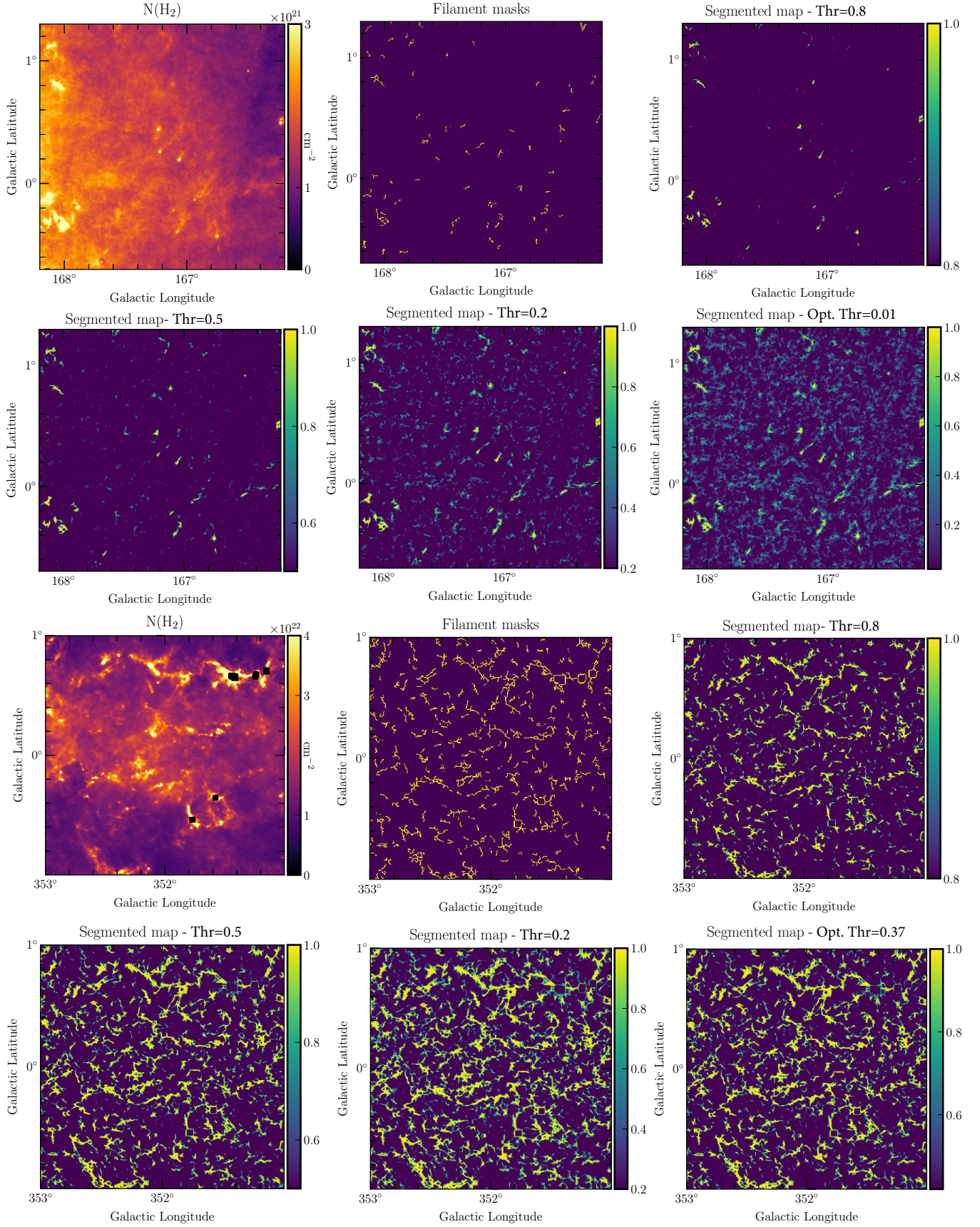


Fig. 18. Zoom-in on the evolution of segmentation results as a function of the classification threshold showing the filamentary structures estimated by UNet++ 10^{-3} in 160–171° (six top images) and 349–356° (six bottom images) regions of the Galactic plane. The original H_2 column density image (top left in each group), the ground-truth input filament mask, and the corresponding segmented image at different thresholds (0.8, 0.5, 0.2, and the optimal threshold) are shown from top left to bottom right. The regions are $2^\circ \times 2^\circ$ wide.

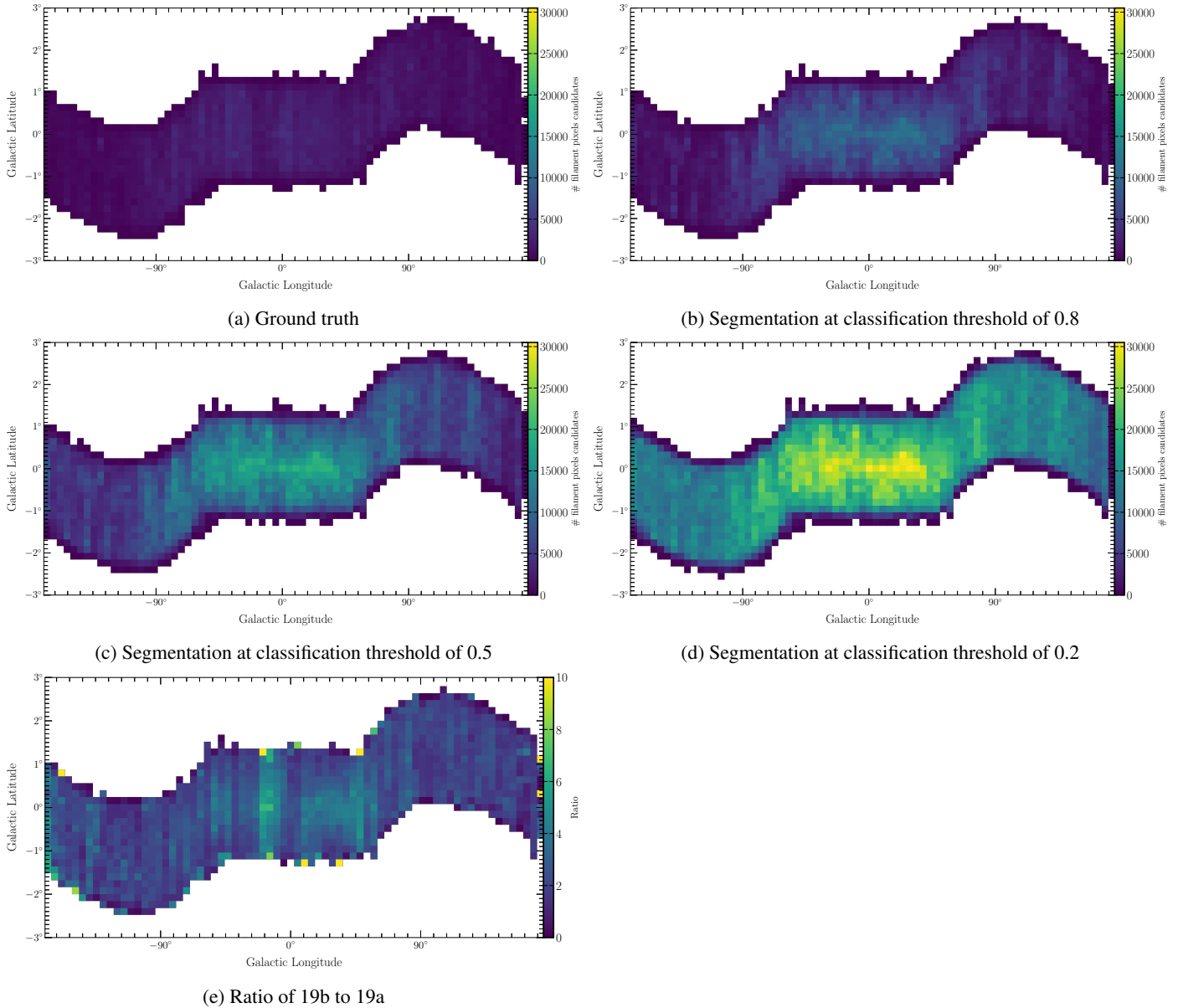


Fig. 19. Number density distribution of candidate filament pixels across the entire Galactic plane, estimated in bins of $4.8^\circ \times 0.16^\circ$ and comparing the ground truth of Fig. 19a with the segmentation results of the model UNet++ 10^{-3} at classification thresholds of 0.8 in Fig. 19b, 0.5 in Fig. 19c, and 0.2 in Fig. 19d. In Fig. 19e, we display the ratio of candidate filament pixels in the segmentation at a classification threshold of 0.8 to the ground truth.

composition, filaments are well visible as absorbing features at shorter wavelengths (optical, near-, and mid-infrared) in the Galactic plane, and these data can be used to ascertain the nature of the structures returned by the training and segmentation processes. Only filaments that are visible in absorption on a strong emission background can be detected at short wavelengths. (Sub)millimeter emission of cold dust also reveals filaments (Mattern et al. 2018; Leurini et al. 2019) and can be used to ascertain the nature of the structures without encountering the extinction problem. This empirical (data-based) validation of the results is a first step in the analysis. In Fig. 22, we illustrate the interest of this multiwavelength analysis to ascertain the nature of new detected filaments on the Galactic region G351.776-0.527. This region hosts a high-mass star-forming region analyzed by Leurini et al. (2019). Region G351.776-0.527 is located at the center of Fig. 22 and appears as a hub with

filaments converging toward the saturated central point located at $l = 351.77^\circ$, $b = -0.538^\circ$. A filamentary structure observed in the segmented map right of the bright central source that is not visible in the input filament mask is seen in the 2MASS K -band image, confirming its nature. The segmented image also suggests that the region might be located at the edge of a bubble. A bright ionized region, G351.46-00.44, is located nearby and could explain the high level of turbulence and the high-mass star formation observed in this zone (Lee et al. 2012). The large-scale view of this region, revealed by the segmented map with suggested multiple filament connections of the central source with the surrounding medium, has to be confirmed with high-sensitivity observations of dust emission that could be complemented by spectroscopic data of dense gas molecular tracers, keeping in mind that, as pointed by Hacar et al. (2022), filaments identified with *Herschel* data (i.e., using dust

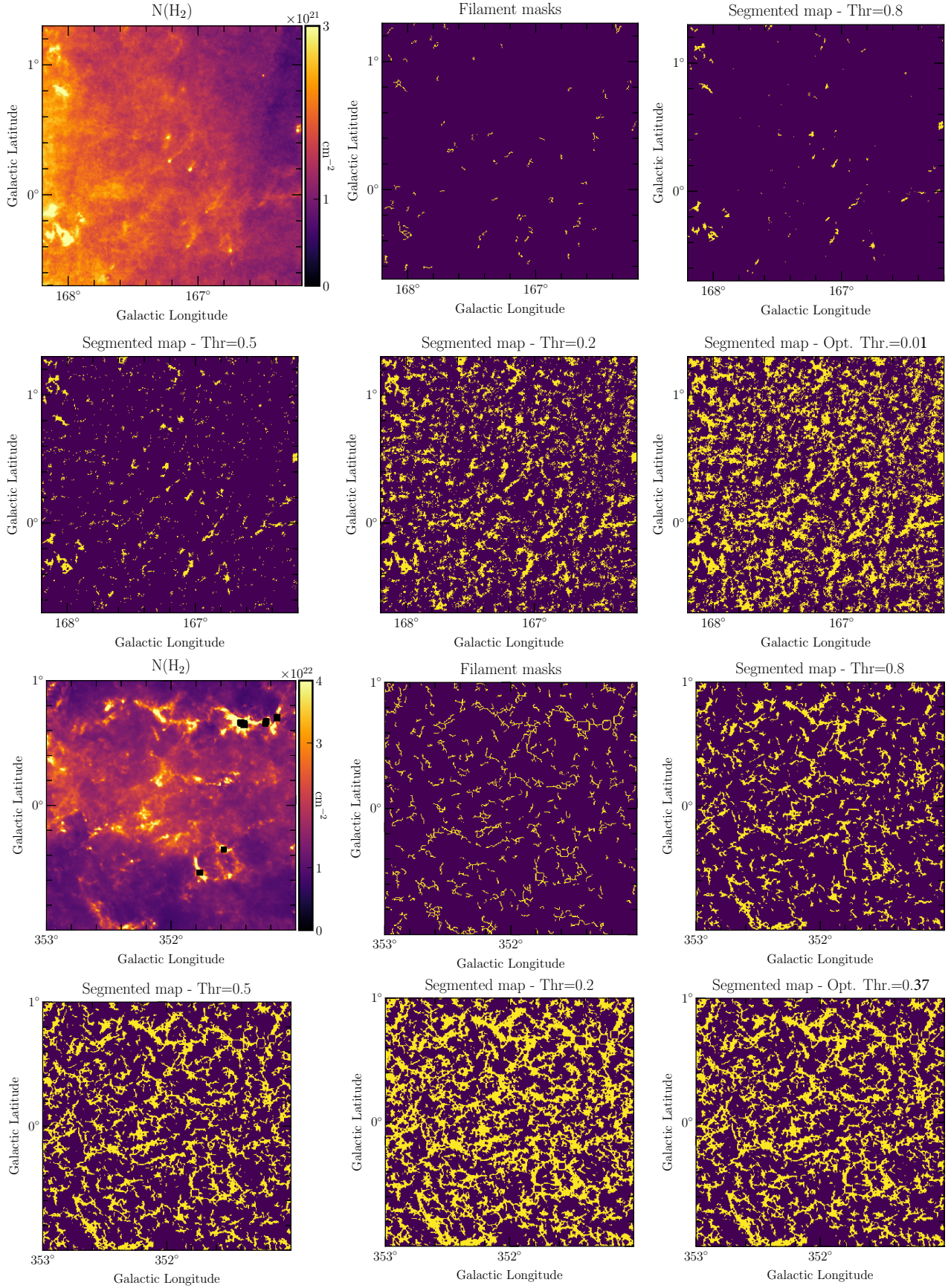


Fig. 20. Zoom-in on the evolution of segmentation results generated by UNet++ 10^{-3} model in mosaics 160–171° (six top images) and 349–356° (six bottom images). Here, the estimated binary filament masks are displayed at classification thresholds 0.8, 0.5, 0.2, and the optimal threshold. The original H_2 column density image (image with the color bar) and the true input filament mask are also displayed for comparison. The regions are $2^\circ \times 2^\circ$ wide.

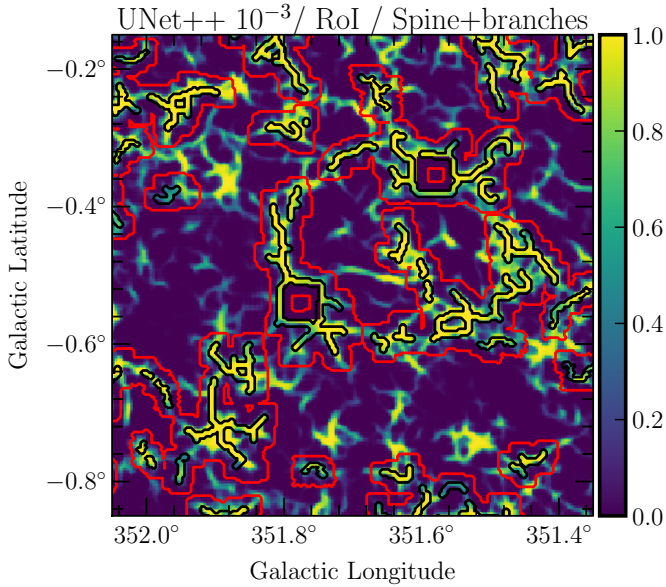


Fig. 21. Comparison of the segmented map result using the UNet++ 10^{-3} with the input spine plus branches (black contours) and the RoI (red contours).

continuum emission) might be a different family of objects than those detected in molecular line tracers.

5. Discussion and future prospects

The purpose of this work was to study the potential of supervised deep learning as a new way to detect filaments in images of the Galactic interstellar medium. At this stage, the filamentary structures are revealed, but the filaments themselves are not extracted, with a measurement of their physical properties, from the segmented images. While the first task requires semantic segmentation, the second task consists of instance segmentation (Gu et al. 2022). In the first, the task is limited to attributing a class to each pixel, which is done in this paper, whereas in the latter, existing filaments are in addition enumerated to allow a global statistical study. In this paper, we used UNet-based networks which are the most modern methods in semantic segmentation. The analyzed performance in Sect. 4 proves the efficiency of these networks not only in revealing structures already existing in the initial catalog, but also in adding new structures that have not been detected before and that are confirmed through a detection at shorter and/or longer wavelengths, namely, at near- and mid-infrared and/or (sub)millimeter wavelengths, respectively. In astrophysics, several independent estimators can be used to ascertain the true nature of the detected filamentary structures, such as expert knowledge or a knowledge based on a large statistical definition, such as the one used in citizen projects, of particular interest for machine learning (Christy et al. 2022). Results of numerical simulations and/or data obtained at other wavelengths can also be used. On the multiwavelength data side, for example, filaments are clearly visible at other wavelengths in the Galactic plane because they are composed of dust, and these data can be used to ascertain the nature of the structures returned by the segmentation process, as shown in Fig. 22.

The UNet-based networks are supervised deep-learning algorithm. In spite of the incomplete ground truth, these networks produced a good estimate of filamentary structures. It is important to build a more enriched ground truth, however, to solve more complex tasks such as instance segmentation. This

Table 6. Training time.

Model	Training time (h)
UNet[10^{-2}]	2.08
UNet[10^{-3}]	2.23
UNet[10^{-4}]	2.19
UNet[10^{-5}]	2.17
UNet++[10^{-3}]	3.22
UNet++[10^{-4}]	2.79
UNet++[10^{-5}]	2.73

Notes. Training time in hours for the schemes reported in Fig. 14. The shortest (longest) training time, in blue (red), is achieved by UNet[10^{-2}] (UNet++[10^{-3}]).

might be possible by combining several existing catalogs of filaments obtained on the Galactic plane, for example, by combining the Hi-GAL catalog (Schisano et al. 2020) with *getSF* extractions made on several regions of the plane (Men'shchikov 2021). Another possibility is to use filament segmentation by UNets as a prestep and then consider the produced filaments mask as the ground truth for the instance segmentation.

Another crucial step in filament segmentation using deep-learning algorithms is data normalization. Filament detection depends not only on the intrinsic column density of the structure, but also on the column density and the structure of the background. By using local (per patch) normalization, the filament contrast relative to the neighboring background is enhanced. As illustrated in Fig. 9, a classical local normalization method was used in this work in order to enhance low-contrast filaments that are in turn well integrated in the training process, allowing them to be representative. Recently, more sophisticated multiscale normalization has been used in the Hi-GAL image processing to highlight the faintest structures observed on the Galactic plane (Li Causi et al. 2016). These normalized data are very interesting as input for deep-learning networks. Unfortunately, no ground truth exists for these normalized images so far, which does not allow their use for the moment.

An important result of the segmentation for astrophysical purposes is to determine the classification threshold (intensity of the segmentation map) that allows for an optimal detection of filaments. While the optimal thresholds reported in Table B.2 allowed a good recovery of existing and new filaments, filaments are still missed at these classification thresholds, some because they were misclassified in the ground truth (see Sect. 4.2).

Another key point is to consider a region-specific optimal threshold rather than a unique global one. According to results reported in Tables 4, 5, and B.2, the optimal threshold of a given model is affected by the column density of the studied zone. In this work, the optimal thresholds in Tables 4 and 5 were inferred in narrow zones, with a low number of labeled pixels for the sparse zone. To obtain a robust estimate of a region-specific optimal threshold, a split of the Galactic plane divided into large homogeneous zones in terms of filament concentration is envisioned. The optimal thresholds can then be inferred on these slices.

From the computational point of view, we trained the different networks on a NVIDIA RTX 2080Ti. Table 6 gives the training time for the different scenarios for 100 epochs. As UNet++ is a larger network than UNet, it takes slightly more time to train: while UNet requires about 2.2 h, UNet++ asks for about 2.8 h. As the patch data set is small (around 210 MB), these

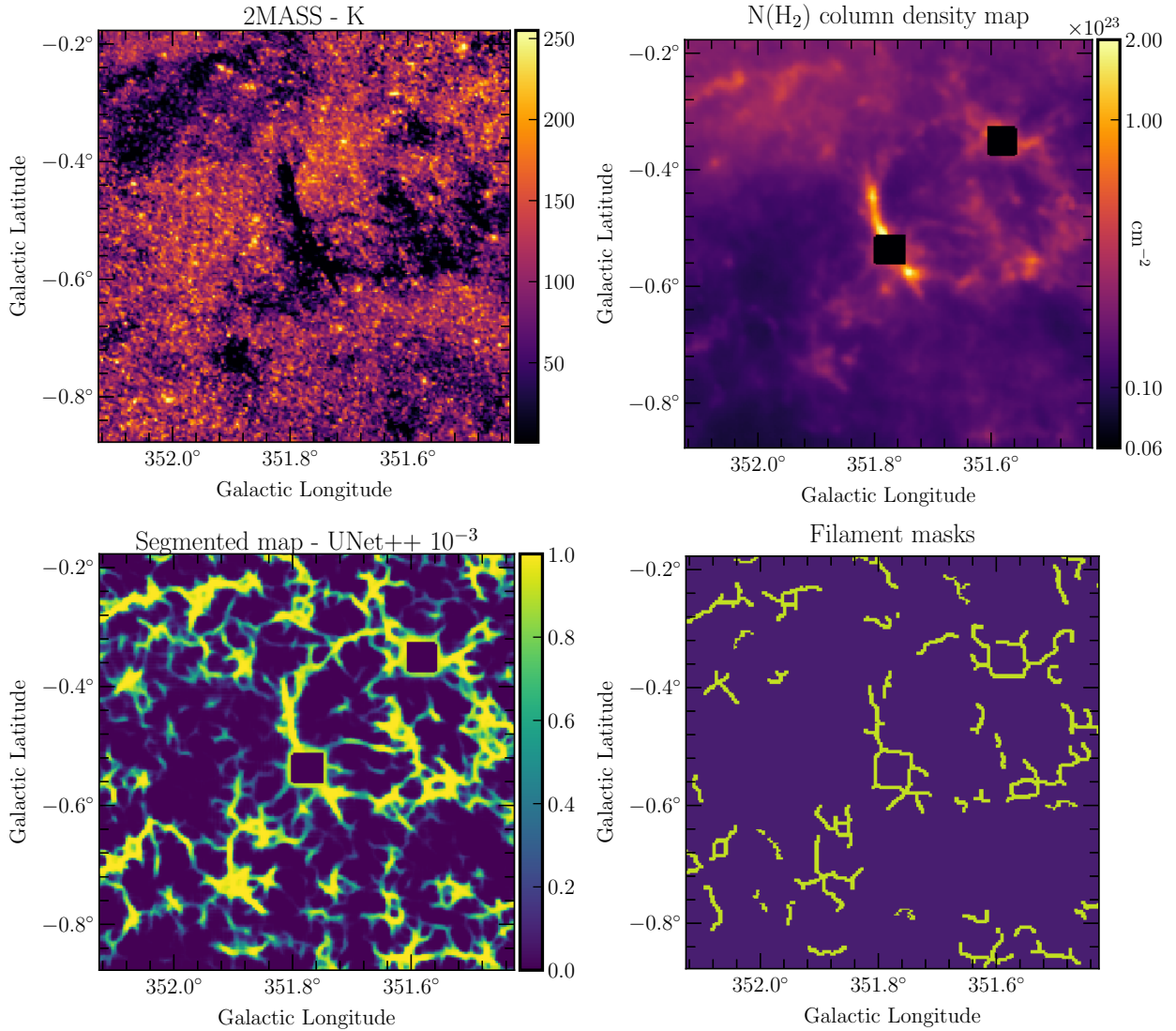


Fig. 22. Segmented map obtained for star-forming region G351.776-0.527 (bottom left) compared with the 2MASS *K*-band image (top left), where filaments are observed in absorption, and the column density map (top right), where filaments are observed in emission. The filamentary structures visible in the image segmented by UNet++ [10–3] (bottom left) and displayed in the [0,1] range are both visible in the 2MASS *K* and N_{H_2} column density images, ensuring their nature. The G351.776-0.527 source is located at the center of the images, connected to a filamentary network (hub). The corresponding input filament mask is shown (bottom right).

times are not impacted by the loading of the data. When the training step is completed, the neural networks are usually faster on CPU than on GPU (Goodfellow et al. 2016) because the transfer from CPU memory to GPU memory takes time. The segmentation of the mosaics was therefore built on an Intel CPU machine (i7-10610U). It took about 4 h per mosaic with an overlap of 30 pixels and 32×32 patches. The total training and segmentation time is therefore estimated to be 6.5 h per mosaic.

From the method point of view, future works will include an improvement of the segmentation process by using dedicated windows to build the patches as in Pielawski & Wählby (2020). These tools may dramatically lower the computational burden. We also investigate alternative ways of building a larger set of patches while keeping good statistical properties. The method used in this work guarantees a good preservation of the statistical distribution, but leads to a small number of patches.

Although this method has some limitations, that is, the limited quantity of patches for the training and the incomplete

ground truth, and although it reveals filament structures instead of extracting them, the net increase (a factor between 2 and 7 on the whole segmented map) of the number of pixels that belongs to the filament class and the robust detection of intrinsically faint and/or low contrast ones offers important perspectives. We currently explore the implementation of an augmented ground-truth data set using results of numerical simulations on Galactic filaments. The extraction and separation of filament pixels observed in the 2D segmented map is also ongoing, and we add 3D spectroscopic data.

6. Conclusions

We explored whether deep-learning networks, UNet-5 and UNet++, can be used to segment images of the whole Galactic plane in order to reveal filamentary structures:

- Using molecular hydrogen column density image of the Galactic plane obtained as part of the Hi-GAL survey and filaments previously extracted by Schisano et al. (2020),

- we trained two different UNet-5 based networks with six different scenarios based on a different initial learning rate.
- We showed the results and estimated the performances of the different scenarios that we presented for two representative mosaics of the Galactic plane selected for their low and high column density density and filament content.
 - We determined the best models for these mosaics based on machine-learning metrics. We focused the training estimates on the recovery of input structures (filaments and background) and defined for each mosaic and for the whole plane an optimal classification threshold that ensured the best recovery of input structures.
 - We show that depending on the model and the selected threshold, new pixels classified as filament candidates increase by a factor between 2 to 7 (compared to the input spine+branches structures used as ground truth). This suggests that this new method has the potential of reveal along filamentary structures that may not be extracted by non-ML-based algorithms.

We point out the high potential of the produced database for future studies of filaments (statistical analysis or follow-ups). We will use the results of the numerical simulations to enrich the ground truth and assess the uncertainties on segmented maps. The astrophysical analysis of the produced database is ongoing and will be published in a separate paper.

Acknowledgements. This project has received financial support from the CNRS through the MITI interdisciplinary programs (Astroinformatics 2018, 2019). This project is part of the ongoing project BigSF funded by the Aix-Marseille Université A*Midex Foundation (SB post-doctoral funding). A.Z. thanks the support of the Institut Universitaire de France. We thank the anonymous referee for their constructive comments that helped to improve the quality of the paper. This research has made use of “Aladin Sky Atlas” developed at CDS, Strasbourg Observatory, France.

References

- Alzahrani, Y., & Boufama, B. 2021, *SN Comput. Sci.*, **2**, 1
- André, P., Men'shchikov, A., Bontemps, S., et al. 2010, *A&A*, **518**, A102
- André, P., Di Francesco, J., Ward-Thompson, D., et al. 2014, in *Protostars and Planets VI*, eds. H. Beuther, R. S. Klessen, C. P. Dullemond, & T. Henning, 27
- Aragon-Calvo, M. A. 2019, *MNRAS*, **484**, 5771
- Arzoumanian, D., André, P., Didelon, P., et al. 2011, *A&A*, **529**, A6
- Arzoumanian, D., André, P., Könyves, V., et al. 2019, *A&A*, **621**, A42
- Batson, J., & Royer, L. 2019, in *International Conference on Machine Learning*, PMLR, 524
- Bekki, K. 2021, *A&A*, **647**, A120
- Bernard, J. P., Paradis, D., Marshall, D. J., et al. 2010, *A&A*, **518**, A88
- Bracco, A., Bresnahan, D., Palmeirim, P., et al. 2020, *A&A*, **644**, A5
- Bianco, M., Giri, S. K., Iliev, I. T., & Mellema, G. 2021, *MNRAS*, **505**, 3982
- Chen, M. C.-Y., Di Francesco, J., Rosolowsky, E., et al. 2020, *ApJ*, **891**, 84
- Christy, C. T., Jayasinghe, T., Stanek, K. Z., et al. 2022, *PASP*, **134**, 024201
- Clarke, S. D., Williams, G. M., & Walch, S. 2020, *MNRAS*, **497**, 4390
- Elia, D., Molinari, S., Fukui, Y., et al. 2013, *ApJ*, **772**, 45
- Fiorio, C., & Gustedt, J. 1996, *Theor. Comput. Sci.*, **154**, 165
- Fu, K.-S., & Mui, J. 1981, *Pattern Recognit.*, **13**, 3
- Fukui, Y., Tokuda, K., Saigo, K., et al. 2019, *ApJ*, **886**, 14
- Goodfellow, I., Bengio, Y., & Courville, A. 2016, *Deep Learning* (MIT Press)
- Gu, W., Bai, S., & Kong, L. 2022, *Image Vis. Comput.*, **120**, 104401
- Hacar, A., Tafalla, M., Forbrich, J., et al. 2018, *A&A*, **610**, A77
- Hacar, A., Bosman, A. D., & van Dishoeck, E. F. 2020, *A&A*, **635**, A4
- Hacar, A., Clark, S., Heitsch, F., et al. 2022, ArXiv e-prints [arXiv:2203.09562]
- Hastie, T., Tibshirani, R., & Friedman, J. 2001, *The Elements of Statistical Learning: Data Mining, Inference, and Prediction*, Springer series in Statistics (Springer)
- Hausen, R., & Robertson, B. E. 2020, *ApJS*, **248**, 20
- He, K., Zhang, X., Ren, S., & Sun, J. 2016, in *2016 IEEE Conference on Computer Vision and Pattern Recognition (CVPR)*, 770
- Hoemann, E., Heigl, S., & Burkert, A. 2021, *MNRAS*, **507**, 3486
- Hsieh, C.-H., Arce, H. G., Mardones, D., Kong, S., & Plunkett, A. 2021, *ApJ*, **908**, 92
- Jadon, S. 2020, *2020 IEEE Conference on Computational Intelligence in Bioinformatics and Computational Biology (CIBCB)*, 1
- Kingma, D. P., & Ba, J. 2015, ArXiv e-prints [arXiv:1412.6980]
- Koch, E. W., & Rosolowsky, E. W. 2015, *MNRAS*, **452**, 3435
- Könyves, V., André, P., Arzoumanian, D., et al. 2020, *A&A*, **635**, A34
- Krizhevsky, A., Sutskever, I., & Hinton, G. E. 2012, *Commun. ACM*, **60**, 84
- Kull, M., Silva Filho, T. M., & Flach, P. 2017, *Electron. J. Stat.*, **11**, 5052
- Kumar, M. S. N., Palmeirim, P., Arzoumanian, D., & Inutsuka, S. I. 2020, *A&A*, **642**, A87
- LeCun, Y., Boser, B. E., Denker, J. S., et al. 1989, *Neural Comput.*, **1**, 541
- Lee, E. J., Murray, N., & Rahman, M. 2012, *ApJ*, **752**, 146
- Lee, C.-Y., Xie, S., Gallagher, P., Zhang, Z., & Tu, Z. 2015, in *Proceedings of Machine Learning Research*, Proceedings of the Eighteenth International Conference on Artificial Intelligence and Statistics, eds. G. Lebanon, & S. V. N. Vishwanathan (San Diego, CA, USA: PMLR), 38, 562
- Leurini, S., Schisano, E., Pillai, T., et al. 2019, *A&A*, **621**, A130
- Li Causi, G., Schisano, E., Liu, S. J., Molinari, S., & Di Giorgio, A. 2016, *SPIE Conf. Ser.*, **9904**, 99045V
- Long, J., Shelhamer, E., & Darrell, T. 2015, in *Proceedings of the IEEE Conference on Computer Vision and Pattern Recognition*, 3431
- Mattern, M., Kauffmann, J., Csengeri, T., et al. 2018, *A&A*, **619**, A166
- Men'shchikov, A. 2021, *A&A*, **649**, A89
- Milletari, F., Navab, N., & Ahmadi, S.-A. 2016, in *2016 fourth International Conference on 3D Vision (3DV)*, IEEE, 565
- Molinari, S., Swinyard, B., Bally, J., et al. 2010, *A&A*, **518**, A100
- Molinari, S., Schisano, E., Elia, D., et al. 2016, *A&A*, **591**, A149
- Oktay, O., Schlemper, J., Folgoc, L. L., et al. 2018, MIDL'18, accepted [arXiv:1804.03999]
- Pielawski, N., & Wahlby, C. 2020, *PLoS One*, **15**, e0229839
- Priestley, F. D. & Whitworth, A. P. 2022, *MNRAS*, **512**, 1407
- Robinson, K., & Whelan, P. F. 2004, *Pattern Recognit. Lett.*, **25**, 1759
- Robitaille, T., Deil, C., & Ginsburg, A. 2020, Astrophysics Source Code Library, [record ascl:2011.023]
- Ronneberger, O., Fischer, P., & Brox, T. 2015, in *International Conference on Medical Image Computing and Computer-assisted Intervention* (Springer), 234
- Schisano, E., Rygl, K. L. J., Molinari, S., et al. 2014, *ApJ*, **791**, 27
- Schisano, E., Molinari, S., Elia, D., et al. 2020, *MNRAS*, **492**, 5420
- Shimajiri, Y., André, P., Ntormousi, E., et al. 2019, *A&A*, **632**, A83
- Soille, P. 2003, *Morphological Image Analysis: Principles and Applications*, 2nd edn. (Berlin, Heidelberg: Springer-Verlag)
- Sousbie, T. 2011, *MNRAS*, **414**, 350
- Traficante, A., Calzoletti, L., Veneziani, M., et al. 2011, *MNRAS*, **416**, 2932
- Vincent, L. 1993, *IEEE Trans. Image Process.*, **2**, 176
- Wells, A. I., & Norman, M. L. 2021, *ApJS*, **254**, 41
- Xia, X., & Kulis, B. 2017, ArXiv e-prints [arXiv:1711.08506]
- Zavagno, A., André, P., Schuller, F., et al. 2020, *A&A*, **638**, A7
- Zhou, Z., Siddiquee, M. M. R., Tajbakhsh, N., & Liang, J. 2019, *IEEE Trans. Med. Imaging*, **39**, 1856
- Zhu, G., Lin, G., Wang, D., Liu, S., & Yang, X. 2019, *Solar Phys.*, **294**, 117
- Zucker, C., & Chen, H. H.-H. 2018, *ApJ*, **864**, 152

Appendix A: Different input data maps

All the input maps used in the training process (the column density map, the filament mask, the background mask, and the missing data mask maps; see Section 2.2) were originally produced from the individual Hi-GAL mosaics extending over 10° of longitude (see Schisano et al. (2020)). To facilitate the use of the four input maps during the training process, we merged the individual maps using the Python module *reproject*¹. The patches were then cut as shown in Figure 4. The four input maps used in the supervised training process are presented in Figure 3. These maps are described below.

N_{H_2} map

The column density maps N_{H_2} were obtained as part of the *Herschel* observations of the Galactic plane, Hi-GAL. The column density N_{H_2} maps were computed from the photometrically calibrated Hi-GAL mosaics following the approach described in Elia et al. (2013). The *Herschel* data were convolved to the $500\ \mu\text{m}$ resolution ($36''$) and rebinned on that map grid. Then a pixel-by-pixel fitting with a single-temperature greybody function was performed, as described in Elia et al. (2013); Schisano et al. (2020). We directly used the data derived and presented in Schisano et al. (2020).

Missing-data map

The N_{H_2} map presents local degraded zones (noise, saturation, and overlap issues) that we wished to exclude from the training process. Examples of these degraded zones are shown in Figure A.1. In Figure A.1 we show the four sources of missing data.

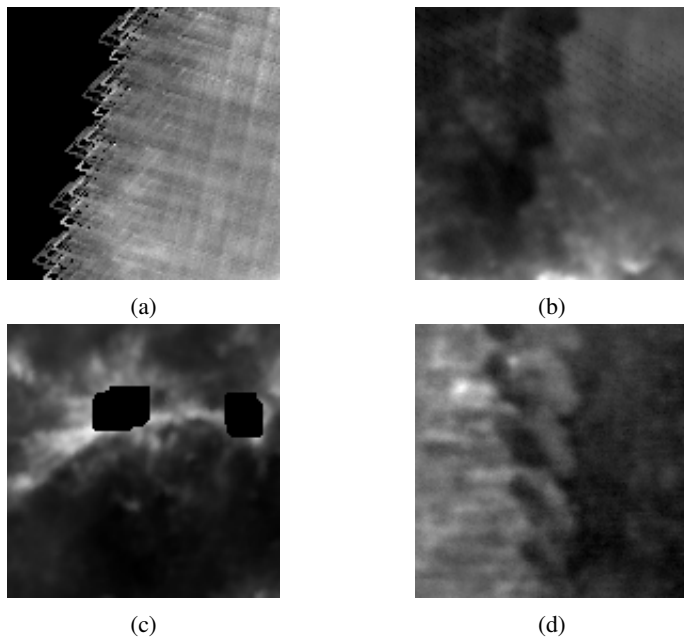


Fig. A.1: Four sources of missing data. (a) Example of a complex boundary due to satellite scanning. (b) Example of a noisy pattern inside the column density map (in log scale) due to the satellite scan. (c) Saturated pixels. (d) Example of structured artifacts built by the mapping process.

¹ <https://reproject.readthedocs.io/en/stable/index.html>

First, the boundaries of the mosaics show a grid-like pattern, as shown in Figure A.1a. These features are due to the scanning pattern followed by the *Herschel* satellite while performing the observations of an Hi-GAL tile. The grid pattern corresponds to the slewing phase of the scanning pattern, when the satellite inverted the scan direction. Second, the Hi-GAL mosaics were built using the Unimap mapmaking (Traficante et al. 2011) following a strategy to avoid large-scale intensity gradients over the image. We refer to Appendix A of Schisano et al. (2020) for a detailed description of how the mosaics were built. In short, UNIMAP mapmaker was run to simultaneously process the data of two adjacent Hi-GAL tiles, creating what the authors call a texel, spanning $4^\circ \times 2^\circ$. The UNIMAP processing is able to deal with the slewing region along the side covered by observation of both Hi-GAL tiles. This produces an image of better quality with respect to the simple mosaicking of the two tiles. Multiple texels are combined together to produce the overall mosaic that is 10° wide in longitude. While it is possible to directly process a larger portion of the Galactic plane with UNIMAP, this approach introduces large gradients in intensity over the entire mosaic. The UNIMAP mapmaker produces maps with an average intensity level equal to zero. Therefore, the texels require to be calibrated in flux (Bernard et al. 2010). In some cases, there are discrepancies in the calibration level of adjacent texels that introduce sharp variations in intensity in the overlapping region between texels. An example is shown in Figure A.1b and Figure A.1d. These variations are not physical and were masked out from the learning process.

The final full map of missing data was built by combining all the types of possible missing data described above. They were then removed from the training.

Filament-mask map

Schisano et al. (2020) published a catalog of filaments detected in the Galactic plane from N_{H_2} images obtained with Hi-GAL photometric data. The position of spines and branches is available through binary masks in which pixels belonging to these structures are tagged for the 32059 filaments published in the catalog (see Figure 2 and their figure 3). We used this information as an input mask to define our ground truth for the filaments. The ground truth was defined over the outputs of the Hi-GAL filament catalog, and it depends on the completeness of that catalog. This implies that the ground truth is not absolutely fully defined because it will miss the information from any feature that may not have been detected by Schisano et al. (2020).

Background map

On all pixels, the column density mosaic contains emission from both filaments and background (Schisano et al. 2020). We examined each 10° mosaic to define a background level as the lowest level of emission observed on the mosaic that does not overlap any filament branches that were detected and used as ground truth. This means that our definition of the background emission sets the background class on a very low number of pixels, but ensures that these pixels do not contain filaments. We work on a more precise definition of the background to allow more pixels to be labeled in this class. We are primarily interested in detecting filamentary structures here. Moreover, the local normalization applied to all patches before the training process (see Figure 9) tends to limit the impact of the background on the detection of filaments. This reduces the need for a precise definition of the background further.

Appendix B: Supplementary quantitative scores

Table B.1: Dice index

Model	Dice index [0.2]	Dice index [0.4]	Dice index [0.6]	Dice index [0.8]
UNet[10^{-2}]	93.19	94.34	94.07	92.06
UNet[10^{-3}]	93.13	94.37	94.16	92.43
UNet[10^{-4}]	92.75	94.09	93.79	91.9
UNet[10^{-5}]	82.4	89.6	91.3	87.66
UNet++[10^{-3}]	93.46	94.61	94.28	92.36
UNet++[10^{-4}]	93.04	94.07	93.6	91.57
UNet++[10^{-5}]	90.24	91.88	91.02	87.67

Notes. Dice index evaluation on the test set for the schemes reported in Figure 14 at classification threshold values of 0.8, 0.6, 0.4, and 0.2. Blue (red) refers to the best (less performing) scheme in each column. The bold scores correspond to the absolute best (if in blue) or lowest (if in red) dice index. The closer the dice index to 1, the better. Dice index values in test were aligned with performances in training and validation steps as close performances are obtained for schemes with initial learning-rate values in [10^{-4} , 10^{-3} , 10^{-2}] and lower performance are noted for schemes with a learning-rate value of 10^{-5} . Moreover, UNet++[10^{-3}] and UNet[10^{-5}] result in the best (94.61% at 0.4) and least performing (82.4% at 0.2) schemes, respectively.

Table B.2: Segmentation scores

Model	UNet [10^{-2}]	UNet [10^{-3}]	UNet [10^{-4}]	UNet [10^{-5}]	UNet++ [10^{-3}]	UNet++ [10^{-4}]	UNet++ [10^{-5}]
Scores (%)							
Precision at 0.8	99.71	99.74	99.75	99.73	99.74	99.74	99.72
Precision at 0.5	98.29	98.45	98.54	97.07	98.47	98.42	97.35
Precision at 0.2	91.43	92.08	91.75	64.85	92.45	91.17	86.16
Precision at thr _{opt}	95.65	95.85	95.88	94.95	95.75	95.94	93.61
Recall at 0.8	72.38	71.34	70.50	65.14	70.87	71.74	65.54
Recall at 0.5	90.13	89.90	89.13	89.25	89.78	89.78	85.59
Recall at 0.2	97.49	97.64	97.29	98.72	97.61	97.50	95.81
Recall at thr _{opt}	95.26	95.50	94.96	92.24	95.67	94.97	91.56
Dice at 0.8	83.88	83.19	82.62	78.81	82.87	83.46	79.10
Dice at 0.5	94.05	94.00	93.62	93.01	93.95	93.92	91.11
Dice at 0.2	94.41	94.82	94.49	78.31	95.01	94.27	90.76
Dice _{opt}	95.46	95.68	95.42	93.58	95.71	95.45	92.57
MS at 0.8	14.36	14.81	16.51	17.58	15.28	15.10	17.69
MS at 0.5	4.61	4.40	5.25	4.07	4.62	4.55	5.83
MS at 0.2	0.83	0.77	0.81	0.28	0.85	0.82	1.10
MS at thr _{opt}	1.95	1.69	1.88	2.72	1.68	1.97	2.85
thr _{opt}	0.32	0.31	0.31	0.44	0.30	0.33	0.34

Notes. Segmentation scores evaluated on the Galactic plane segmented by the models reported in Figure 14. Precision, recall, dice index, and MS rate are evaluated at classification threshold values of 0.8, 0.5, 0.2, and the optimal threshold. The latter refers to the threshold value optimizing the dice index and estimated using P-R curves (see Figure 15c). Blue (red) refers to the best (least performing) scheme in each row. The bold scores correspond to the absolute best (if in blue) or lowest (if in red) performance per score. Overall, the segmentation scores obtained on the fully segmented Galactic plane consolidate the results obtained with the zone of 350.3-353.5° in Table 4